Title	Similarities of artificial photosystems by ruthenium oxo complexes and native water splitting systems.
Author(s)	Tanaka, Koji; Isobe, Hiroshi; Yamanaka, Shusuke; Yamaguchi, Kizashi
Citation	Proceedings of the National Academy of Sciences of the United States of America (2012), 109(39): 15600-15605
Issue Date	2012-09-25
URL	http://hdl.handle.net/2433/160397
Right	©2012 by the National Academy of Sciences
Type	Journal Article
Textversion	author

Similarities of Artificial Photosystems by Ruthenium Oxo Complexes and Native Water Splitting Systems between Artificial and Native Water Splitting Systems

Koji Tanaka [a,b], Hiroshi Isobe[c], Shusuke Yamanaka[c], Kizashi Yamaguchi[d]

[a]Institute for Integrated Cell-Material Sciences, Kyoto University, Funai Center #201, Katsura, Nishikyo-ku, Kyoto 615-8530, Japan
[b]Institute for Molecular Science, 5-2, Higashiyama, Okazaki, 444-8787, Japan
[c]Graduate School of Science, Osaka University, Toyonaka, 560-0043, Japan
[d]TOYOTA Physical & Chemical Research Institute, Nagakute, Aichi 480-1192, Japan

Abstract

The nature of chemical bonds of ruthenium(Ru)–quinine(Q) complexes, mononuclear $[Ru(trpy)(3,5\text{-t-}Bu_2Q)(OH_2)](ClO_4)_2$ (trpy=2,2':6',2''-terpyridine, 3,5-di-tert-butyl-1,2-benzoquinone) (**1**), and binuclear $[Ru_2(btpyan)(3,6\text{-di-}Bu_2Q)_2(OH_2)]^{2+}$ (btpyan = 1,8-bis(2,2':6',2''-terpyrid-4'-yl)anthracene, $3,6\text{-t-}Bu_2Q$ = 3,6-di-tert-butyl-1,2- benzoquinone) (**2**) has been investigated by broken-symmetry (BS) hybrid density functional (DFT) methods. BS DFT computations for the Ru complexes have elucidated that the closed-shell structure (**2b**) Ru(II)–Q complex is less stable than the open-shell structure (**2bb**) consisted of Ru(III) and semiquinone (SQ) radical fragments. These computations have also elucidated eight different electronic and spin structures of tetraradical intermediates may be generated in the course of water splitting reaction. The Heisenberg spin Hamiltonian model for these species has been derived to elucidate six different effective exchange interactions (J) for four spin systems. Six J values have been determined using total energies of the eight (or seven) BS solutions for different spin configurations. The natural orbital analyses of these BS DFT solutions have also been performed to obtain natural orbitals and their occupation numbers that are useful for lucid understanding of the nature of chemical bonds of the Ru complexes. Implications of the computational results are discussed in relation to propose reaction mechanisms of water splitting reaction in artificial photosynthesis systems and similarity between artificial and native water splitting systems.

/body

Introduction

Photosynthesis is one of the most important chemical processes in our planet. Extensive experimental studies (1-6) on the process have revealed that oxygenic photosynthesis involves several protein-cofactor complexes embedded in the photosynthetic thylakoid membranes of plants, green algae and cyanobacteria. Among these complexes, photosystem II (PSII) has a prominent role because it catalyzes the oxidation of water ($2H_2O \rightarrow O_2 + 4H^+ + 4e^-$) that is the prerequisite for all aerobic life. The main cyclic process to catalyze the water-oxidation consists of successive four steps; this is referred to as the so-called Kok cycle (6). During this process, the oxygen-evolving complex (OEC), which is the catalyst of the water oxidation reaction, takes five oxidation states (S_0-S_4). The OEC in PSII contains an inorganic cluster consisted of four manganese ions and one calcium ion that are bridged by at least five oxygens: the active site is therefore expressed with the $CaMn_4O_5$ cluster (**3**) (5). Very recently the electronic structure and reactivity of **3** (7-10) have been elucidated based on the new high-resolution X-ray structure (5).

Past decades, a number of experimental and theoretical studies (11-29) have been performed to design artificial photosynthetic systems that mimic native PSII systems. Many binuclear transition-metal catalysts such as $L(H_2O)M$-O-$M(OH_2)L$ or $L(H_2O)$ M(BL)-$M(OH_2)$ (where L and BL are nonbridging and bridging organic ligands, respectively) were prepared and characterized for their catalytic properties toward water oxidation (11-21). By combining structural and kinetic studies, impressive progress has been achieved in unraveling the molecular mechanism of the catalytic action of the so-called blue dimmer (12), [cis,cis-$(bpy)_2(H_2O)$Ru-O-$Ru(OH_2)(bpy)_2$](bpy=2,2’- bipyridine); however, the detailed mechanism of the final stage of the O-O bond formation and O_2 evolution remains unsettled despite several theoretical investigations (22-24, 26, 28); radical coupling and acid-base mechanisms for the oxygen-oxygen (O-O) bond formations are still competitive.

On the other hand, Tanaka and coworkers (16-21) have reported water oxidation catalytic activity of Ru-quinone complexes: mononuclear [Ru(trpy)(3,5-t-Bu_2Q)(OH_2)]$(ClO_4)_2$ (trpy = 2,2’:6’,2”-terpyridine, 3,5-t-Bu_2Q = 3.5-di-tert-butyl-1,2- benzoquinone) (**1**) and binuclear [Ru_2(btpyan)(3,6-di-$Bu_2Q)_2(OH_2)$]$(SbF_6)_2$ (btpyan = 1,8-bis (2,2’:6’,2”-terpyrid-4’-yl) anthracene, 3,6-di-Bu_2Q = 3,6-t-Bu_2Q_2 (3,6-di-tert- butyl -1,2- benzoquinone) (**2**). Recently Muckerman, Fujita, and Tanaka et al (25), and Ghosh and Baik (27) have performed density functional (DFT) calculations of these Tanaka catalysts. However, computational results by these groups are different on the relative stability between the closed-shell and open-shell structures (see section II. 1 and supporting materials) of **1** and **2**.

Here, we perform broken-symmetry (BS) DFT computations of the above mononuclear (**1**) and binuclear (**2**) Tanaka catalysts. Eight different electronic and spin structures are calculated for tetraradical intermediates generated in the course of water splitting reaction by **2**. The Heisenberg spin Hamiltonian model for the species is derived to elucidate six different effective exchange interactions (J) for four spin systems (7-10). Six J values are determined using total energies of the eight (or seven) BS solutions for different spin configurations. The natural orbital analyses of these BS DFT solutions are also performed to elucidate natural orbitals and their occupation numbers that are utilized for MO-theoretical explanation of the nature of chemical bonds of **2**. Implications of the computational results are discussed in relation to reaction mechanisms proposed for water splitting reaction in artificial photosynthesis systems and similarity between artificial and native water splitting systems.

II. Results

II.1 Possible electronic and spin states of mononuclear and binuclear ruthenium quinone complexes

Dioxolene, dithiolene and benzoquinodiimine have been accepted as non-innocent ligands in transition-metal complexes that often exhibit catalytic activity. The notable point in the catalysts reported by Tanaka et al. (16-21) is that quinone is used as redox-active ligands. In fact, various mixed-valence structures have been proposed for active valence states of the mononuclear Ru complex (**1**), [Ru(II)(3,5-tertially-butyl quinone; t-BuQ)(terpyridyl; tpy)X] (X = H_2O, OH^- and O^{2-}), as illustrated in Fig. 1. Although the Ru complex (**1**) synthesized by Tanaka et al [16-21] is formally regarded as a closed-shell species, Ru(II)(t-BuQ)(tpy)(H_2O) (**1a**) (Figure 1), thermal one-ET from the HOMO(D) of Ru(II) to the LUMO(A) of t-BuQ is theoretically conceivable, providing the for •Ru(III)(t-BuSQ•)(tpy)(H_2O) diradical structure (**1aa**). On the other hand, contribution of the double ET (DET) structure Ru(IV)(t-BuCat)(tpy)(H_2O) (**1aaa**) is usually neglected. Relative contributions of **1a** and **1aa** are highly dependent on substituents introduced into quinone skeleton and environmental conditions employed because the HOMO(D)-LUMO(A) gaps are sensitive to them. The situation is the same even for the deprotonated structures, Ru(II)$(tBuQ)_2$(tpy)(OH^-) (**1b**), and one- and double-ET from Ru(II) to tBuQ afford •Ru(III)$(tBuSQ\bullet)_2$(tpy)(OH^-) (**1bb**) and Ru(IV)$(tBuCat)_2$(tpy)(OH^-) (**1bbb**), respectively. Further deprotonation of **1b** provides a formal closed-shell structure, Ru(II)(tBuQ)(tpy)(O^{2-}) (**1c**). One ET from the HOMO(D) of oxygen dianion (O^{2-}) to the LUMO(A) of quinone is feasible to generate the triplet diradical structure, Ru(II)(tBuSQ-•)(tpy)(O^-•)(**1cc**). The closed-shell configuration of **1c** (Fig. 1) becomes unstable than open-shell ET configuration of **1cc** (Fig. 1), indicating that the ET diradical state becomes the ground state (see Fig. S1(C)).

Fig. 1

The effective exchange integral (J) between t-BuQ-• and O^-• radicals is positive (ferromagnetic) because of the orbital orthogonality. Tanaka et al [18] have indeed concluded that the observed species by the ESR spectroscopy can be assigned to be the triplet state of **1cc**, and a visible absorption band at 870 nm is assigned as MLCT of **1cc** (see Fig. S2(B)). On the other hand, deprotonation of **1bb** provides an open-shell structure, •Ru(III)(tBuSQ•)(tpy)(O^{2-}) (**1d**). One ET from the HOMO(D) of oxygen dianion (O^{2-}) to the LUMO(A) of SQ of **1d** provides another mixed-valence triplet structure •Ru(III)(tBuCat)(tpy)(O^{-}•) (**1dd**). The effective exchange integral (J) between Ru(III)• and O^{-}• radicals is also positive because of the orbital orthogonality (Hund rule). One electron oxidation of **1cc** provides a free radical doublet structure, Ru(II)(tBuQ) (tpy)(O^{-}•↑) (**1e**) in Fig. 1. One ET (OET) from HOMO(D) of Ru(II) to LUMO(A) of quinone of **1e** provides **1ee**. One electron oxidation of **1d** and **1dd** also affords the same triradical species, ↑•Ru(III)(tBuSQ•↓)(tpy)(O^{-}•↑) (**1ee**). The high-valent free radical species, Ru(IV)(tBuCat)(tpy)(O^{-}•) (**1eee**) is also conceivable via one more OET, though it may be too unstable. The radical coupling for the O-O bond formation may be feasible for radical species with an oxyl-radical site, **1cc**, **1dd**, **1e** and **1ee**.in Fig. 1. Indeed, Tanaka et al [34] have demonstrated experimentally that **1ee** can abstract hydrogen atom of organic substrates but **1cc** does not have such activity.

Tanaka et al. (20,21) have synthesized a dimer (**2**) of the mononuclear Ru complex (**1**), [Ru(II)$_2$(3,6-t-BuQ)$_2$(btpyan)X$_2$]$^{n+}$ (btpyan = 1,8-bis(2,2':6',2''-terpyridyl anthracene, X = H$_2$O, OH^{-} and O^{2-}), which can electrocatalytically oxidize water to produce molecular oxygen. On the basis of various experimental results such as CV and UV–visible spectra, Tanaka et al. (21) have proposed simple reaction pathways for the O-O bond formation that is a crucial step for water splitting reaction: **2b** → **2bcc** → **2cc** → **2f** **(**peroxide) in methanol and **2b** → **2cc** → **2f** **(**peroxide) in water as shown in Fig. 2A. The stepwise deprotonation of **2b** by base (tBuOK) entails an intermediacy of an unsymmetrical mixed structure **2bcc =** [(**1b**)(**1cc**)] in methanol, while spontaneous deprotonation of **2b** in water directly afford **2cc**. The radical coupling between oxyl-radicals has been assumed for the O-O bond formation in **2f (**peroxide).

Fig. 2

On the other hand, Ghosh and Baik (27) have presented a different pathway involving electron-transfer configurations: **2b → 2bb → X → 2cc → 2f (**peroxide) in methanol as shown in Fig. 2B. They have emphasized an important role of **2bb** (double OET structure) and a mixed valence intermediate (**X**) based on the DFT computational results. However, the radical-coupling step by their model is the same with that of Tanaka reaction path model in Fig. 2A. They have also proposed a possible role of the unsymmetrical polar structure **2a(+)ee** in water: **2b** ® **2a(+)ee** ® **2ee**. Thus the proposed mechanisms by Tanaka et al (21) and Ghosh and Baik (27) are the radical-coupling type instead of polar ionic mechanism even in water.

DFT computations by Muckerman, Fujita and their coworkers (25) have indicated that possible contribution of one ET configuration **2bb** = [(**1b**)(**1b**)] is scarce in accord with their experimental results, though early papers by Tanaka group have proposed one ET structure **2bb** on the basis of the X-ray diffraction and spectroscopic observations (16). However, Muckerman et al. (25) have noticed that contribution of **2bb** increases with introduction of electron-withdrawing substituents like chlorine into quinone skeletons. Muckerman et al. (25)

have proposed a possible reaction pathway involving intermediacy of Ru-superoxide anion complex for water splitting reaction: **2b** ® **Y** as shown in Fig. 2A. The intermediate **Y** is consisted of **1b** and **1cc**, namely **2bcc =** [(**1b)(1cc**)], and the O-O bond formation between hydroxy anion (-HO-Ru(II)-Q: **1b**) and oxyl radical (-•O-Ru(II)-SQ•: **1cc**) has been assumed at this step. The superoxide complex [SQ•-Ru(II)-(-•O-O)-Ru(II)-Cat] is formed via deprotonation at the O-O bond formation step because quinone (Q) accept excess two electrons, forming chatecholate (Cat) as illustrated in Fig. 2A. The valence of Ru ion remains to be divalent throughout water activation processes for the O-O bond formation.

In the proposed mechanisms mentioned above (21,25,27), **2bb** and **2a(+)ee** are assumed to be key redox intermediates during catalysis leading to the O–O bond formation. Notably, these four-site four-spin systems are analogous to the $CaMn_4O_5$ (**3**) cluster in OEC of PSII (7-10). Therefore we have investigated in detail electronic and spin structures and magnetic interactions of the binuclear ruthenium quinone complexes **2bb** and **2a(+)ee** (X = H) by assuming the geometries optimized by Ghosh and Baik (27). There are eight different spin configurations for the four-site spin systems, as illustrated in Fig. 3, where the notations (abcd) or (4321) means the sites (SQ_2)(Ru_2)(Ru_1)(SQ_1) for **2bb** and (SQ_2)(O_1)(Ru_1)(SQ_1) for **2a(+)ee**, in conformity with the notation of OEC, Ca($Mn_{a(4)}$)($Mn_{b(3)}$)($Mn_{c(2)}$)($Mn_{d(1)}$). We have constructed eight broken-symmetry (BS) solutions by the B3LYP method with the double-ζ LANL2DZ(Ru)/6-31G*(C,H,O,N) basis set implemented in Gaussian 09 (30). Table 1 summarizes relative energies of the open-shell configurations (**2bb** and **2a(+)ee**) with reference to the closed-shell (CS) configuration (**2b**); Mulliken spin densities of **2bb** and **2a(+)ee** are given in Tables S1 and S2.

As for **2bb**, the antiferromagnetic (AF) configuration (↓•SQ_2)(↑•Ru_2)(↑•Ru_1) (↓•SQ_1) (^{1}H) is the most stable among the eight BS states. But the other AF configuration (↑•SQ_2)(↓•Ru_2)(↑•Ru_1)(↓•SQ_1) (^{1}G) is almost degenerated in energy: the energy gap of this group is about -12 kcal/mol. The next stable group is given by the triplet configurations: (↓•SQ_2)(↑•Ru_2)(↑•Ru_1)(↑•SQ_1) (^{3}B) and (↑•SQ_2)(↓•Ru_2)(↑•Ru_1) (↑•SQ_1) (^{3}C): the energy gap is about -10 kcal/mol. The other triplet group: (↑•SQ_2)(↑•Ru_2)(↑•Ru_1)(↓•SQ_1) (^{3}E) and (↑•SQ_2)(↑•Ru_2)(↓•Ru_1)(↑•SQ_1) (^{3}D) provides the energy gap = -8.3 kcal/mol. The gap is about -6.4 kcal/mol for the group of unstable tetraradical species: (↑•SQ_2)(↑•Ru_2)(↑•Ru_1)(↑•SQ_1) (^{5}A) and (↓•SQ_2)(↓•Ru_2)(↑•Ru_1) (↑•SQ_1) (^{1}F). Thus the energy gaps for the eight BS configurations of **2bb** are not so large, indicating labile electronic chemical bonds of Tanaka catalysts [16-21].

Fig. 3, Table 1

Concerning the polar structure **2a(+)ee**, the antiferromagnetic (AF) configuration (↓•SQ_2)(↑•O_1)(↑•Ru_1)(↓•SQ_1) (^{1}H) is the most stable among the eight BS states. But the triplet configuration (↑•SQ$_2$)(↑•O$_1$)(↑•Ru$_1$)(↓•SQ$_1$) (^{3}E) is almost degenerated in energy: the energy gap of this group is about -5 kcal/mol. The next stable group is given by the configurations: (↑•SQ$_2$)(↑•O$_1$)(↑•Ru$_1$)(↑•SQ$_1$) (^{5}A) and (↓•SQ$_2$)(↑•O$_1$)(↑•Ru$_1$)(↑•SQ$_1$) (^{3}B): the energy gap = -3.1 kcal/mol. The unstable group: (↑•SQ$_2$)(↑•O$_1$)(↓•Ru$_1$)(↑•SQ$_1$) (^{3}D) and (↑•SQ$_2$)(↓•O$_1$)(↑•Ru$_1$)(↓•SQ$_1$) (^{1}G) provides the positive energy gap = 1.0 kcal/mol. The gap becomes about 3.7 kcal/mol for the group of further unstable tetraradical species: (↓•SQ$_2$)(↓•O$_1$)(↓•Ru$_1$)(↑•SQ$_1$) (^{1}F) and (↑•SQ$_2$)(↓•O$_1$)(↑•Ru$_1$) (↑•SQ$_1$) (^{3}C). Thus the energy gaps for the eight BS configurations of **3a(+)ee** are not so large, indicating labile electronic chemical bonds of Tanaka catalysts.

II.2. Heisenberg spin Hamiltonian model and spin vector model

Magnetic measurements have been performed for a number of exchange- coupled systems. The Heisenberg spin Hamiltonian model has been employed for the analysis of experimental results available. In order to elucidate similarity between the Tanaka catalyst **2** and CaMn$_4$O$_5$ (**3**), we here consider the model Hamiltonian for four-site four-spin systems like **2bb** and **2a(-)ee** examined above. The Heisenberg spin Hamiltonian for the systems is given by eqs. (S16) and (S17). Therefore the expectation value for the spin Hamiltonian is given on the quantum mechanics in eq. (S18). The expectation values of the Heisenberg spin Hamiltonian are often approximated on the assumption that local spins are regarded as classical (axial) spin (vector). Here the up- and down-spin vectors are considered in accord with BS calculations of the different-orbitals-for-different-spins (DODS) type. Then the expectation values of the classical Heisenberg model are given by (7-10)

$$
\begin{aligned}
<\mathbf{H}>_C = & -J_{ab}S_{ab}{}^2 - J_{ac}S_{ac}{}^2 - J_{ad}S_{ad}{}^2 - J_{bc}S_{bc}{}^2 - J_{bd}{}^2 S_{bd}{}^2 - J_{cd}S_{cd}{}^2 \\
& + S_a{}^2 (J_{ab} + J_{ac} + J_{ad}) + S_b{}^2 (J_{ab} + J_{bc} + J_{bd}) \\
& + S_c{}^2 (J_{bc} + J_{cd} + J_{ac}) + (J_{cd} + J_{ad} + J_{bd})
\end{aligned}
\quad , \qquad (1)
$$

where S$_i$ and S$_{ij}$ are spin quantum numbers of quantum spin i and spin pair (ij) in eq. (S17), respectively. J_{ab} denotes the effective exchange integral between sites a and b as shown in Fig. 3. J_{ab} values can be determined by electron spin resonance (ESR) [18] and other magnetic measurements.

We can construct simultaneous equations for J values from the total energies of eight BS solutions examined in the section II.1, as shown in eqs (S21a) and (S21b). By solving these equations, we can obtain all J values, as summarized in Table 2. As expected energy levels in section II.1, J$_{ab}$ and J$_{cd}$ for **2bb** (-3.77 and -1.88 kcal/mol, respectively) are negative in sign, indicating the greater stability of the singlet pairs. However, the magnitude is considerably different in accord with the unsymmetrical electronic state as shown below. As for **2a(+)ee**, J$_{bc}$

is largely positive in sign, indicating the greater stability of the triplet pair (↑•O_1)(↑•Ru_1). The singlet-triplet gap for this pair is about J=6.4 kcal/mol under the BS approximation. However, spins in molecules are the angular momentums described by quantum mechanics. Therefore the above classical approximation in eq. (1) is a drastic approximation. We can determine the quantum corrections using the ($\mathbf{S}_t^2$) values by the UB3LYP calculations as shown in supporting materials. Table 2 summarizes the quantum-corrected J values after the approximate spin projection (AP) that eliminates the spin contamination in the BS solution (7-10). The AP correction is not negligible for the AF exchange integrals, J_{ab} and J_{cd}, because the size of local spin is 1/2 in **2bb** and **2a(+)ee** .

Table 2

The energy gaps for key species after AP correction are summarized in Table 1. The energy gaps between closed-shell **2b** and open-shell **2bb** before and after AP are 12.0 and 15.4 kcal/mol, indicating a non-negligible correction (3.4 kcal/mol). On the other hand, the energy gaps between **2b** and **2a(+)ee** before and after AP are 5.0 and 6.3 (kcal/mol). The very large corrections are necessary for ^{3}C, ^{3}D, ^{1}F and ^{1}G states of **2a(+)ee**. This is attributable to the large J_{bc} value (=6.4 kcal/mol). For lucid understanding of AP correction, let us consider the •O-R(III)• biradical (**1dd** in Fig. 1) as shown in Fig. S3. The singlet-triplet (S-T) energy gap for **1dd** is about 6.4 (=J_{bc}) kcal/mol by the BS UB3LYP calculation but it becomes about 12.3 (=2J_{bc}) kcal/mol after AP correction. The gap after AP is smaller than the isoelectronic molecular oxygen (22.4 kcal/mol; note that the BS energy gap is 11 kcal/mol) (31) and that of the iron-oxo species (about 14 kcal/mol) (32), although the latter value for the three-spin system is regarded as the energy of the equal mixture of local singlet and triplet states (33). On the other hand, the S-T gaps for OH-Ru(III)•-SQ• biradical (**1aa** and **1bb** in Fig. 1) becomes about 4 and 6 kcal/mol before and after AP as shown in Fig. S3. The ground state of •O-R(II)-SQ• biradical (**1cc** in Fig.1) is triplet (J_{bd} >0) in accord with the ESR experiment by Tanaka et al (16, 18).

The J values in Table 2 are applicable to estimate energy gaps for a triradical species: the •O-Ru(III)•-SQ• radical (**1ee** in Fig. 1). There are four spin alignments for **1ee**: A(↑•O-Ru(III)•↑-SQ•↓)，B（↑↑↑），C（↑↓↑）and D（↓↑↑）. The relative energies for A(↑↑↓)，C（↑↓↑）, and D（↓↑↑）setting the ferromagnetic state B（↑↑↑）as the reference are, respectively, -1.91, 4.03 and 6.78 (kcal/mol) under the BS approximation. On the other hand, they become -7.63, 8.24 and 13.12, (kcal/mol) after quantum correction by AP. The significant correction energies are attributable to the large J_{bc} value (=6.4 kcal/mol) as in the case of **2a(+)ee** in Table 1. These energy gaps for **1ee** are used to estimate the energy gaps for hexaradical species: dimmer of **1ee** in Fig. 1 (•SQ-Ru(III)•-O• •O-Ru(III)•-SQ•). Fig. S4 illustrates possible spin alignments for the hexaradical species **1ee-1ee**. The ground spin configurations: ^{3}A(↓↑↑↑↑↓) and ^{1}A(↓↑↑↓↓↑) are nearly degenerated in energy because the effective exchange coupling between the oxygen radicals (O• •O) is weak. The first excited configurations: ^{7}B(↑↑↑↑↑↑) and ^{1}B(↑↑↑↓↓↓) are consisted of the ferromagnetic spin alignment of the monomer (**1ee**). The energy gap between the ground and the first excited states are about 3.8 and 6.4 (kcal/mol) before and after AP as illustrated in Fig. S4. The energy diagram in Fig. S4 can be applicable for examination of possible reaction pathways for water splitting reaction.

III. Discussion

III.1. Natural orbital analysis of BS solutions

Present UB3LYP calculations have elucidated that one electron transfer (OET) configuration from HOMO of Ru(II) to the LUMO of quinone plays an important role to generate four spin sites denoted as (SQ_2,Ru_2, Ru_1,SQ_1) (**2bb**). Therefore eight spin structures are feasible as shown in Fig. 3, where (SQ_2,Ru_2,Ru_1,SQ_1) (**2bb**) is expressed by (abcd) as in the case of native water splitting enzyme: $CaMn_{a(4)}$ $Mn_{b(3)}Mn_{c(2)}Mn_{d(1)}$(**3**) in photosystem II (7-10). The same spin Hamiltonian model has been derived to elucidate similarity between artificial (**2bb**) and native (**3**) catalysts for water splitting reaction, though the size of local spin is different between **2bb** (size of each spin =1/2) and **3** (size of each spin =4/2 for Mn(III)). However, as shown in the previous natural orbital analysis of BS solutions for **3**, the magnetic local spins in three t_{2g} orbitals of each Mn(X) (X=III, IV) ions are almost intact for the O-O bond formation. This means that local spin (s=1/2) in e_g orbital of Mn ion plays an important role for formation of labile Mn-O bond (7-10), indicating the similarity between **2bb** and **3**.

The natural orbital analysis of the BS solution is useful for elucidation of effective exchange interactions of active electrons in **2bb**. Fig. S5 shows natural orbitals (NO) and their occupation numbers for the antiferromagnetic spin configuration (↓•SQ_2)(↑•Ru_2)(↑•Ru_1)(↓•SQ_1) (^{1}H in Fig. 3) of **2bb**. The HONO and LUNO are delocalized orbitals, and their mixing provides more or less localized (diradicaloid) orbitals. The orbital overlaps for diradicaloid (frontier) orbitals for (↑•Ru_1)(↓•SQ_1) and (↓•SQ_2)(↑•Ru_2) are 0.40 and 0.55, respectively, as shown in Fig. S5. Therefore the effective exchange interaction between the former pair is about one-half of the latter pair because the magnitude of J is roughly parallel to the square of the orbital overlap: $(0.4)^2/(0.55)^2=J_{cd}/J_{ab}=0.16/0.30= 1.88(1.61)/3.77(2.89)$. Thus the left and right pairs of **2bb** are not equivalent, namely breaking of cluster symmetry in the electronic state.

The proton-coupled electron transfer may be feasible for **2bb** to afford the unsymmetrical structure **2a(+)ee**. Fig. S6 illustrates NOs and their occupation numbers for the antiferromagnetic spin configuration (↓•SQ_2)(↑•O_1)(↑•Ru_1)(↓•SQ_1) (^{1}H in Fig. 3) of **2a(+)ee**. The complete mixing of HONO and LUNO affords localized orbitals for the former pair. In fact, the orbital overlaps for the active orbitals for (↓•SQ_2)(↑•O_1) and (↑•Ru_1)(↓•SQ_1) are 0.00 and 0.38, respectively. The effective exchange interaction for the (↓•SQ_2)(↑•O_1) pair is essentially zero (complete diradical) because of zero orbital overlap. The local spin on the O_1 site is expected to show high radical reactivity. On the other hand, the orbital overlap (0.38) for the (↑•Ru_1)(↓•SQ_1) pair is almost the same (0.40) as that of **2bb**. Thus the natural orbital analysis provides a lucid MO-theoretical explanation of exchange-coupled electrons in Tanaka catalysts.

III.2. Radical coupling and nonradical mechanisms for the O-O bond formation

Accumulated experimental and theoretical studies (11-29) on artificial photosynthesis systems have elucidated dual possible mechanisms of water splitting reaction: (A) radical coupling (RC) mechanism and (B) acid-base mechanism. Tanaka et al. have proposed the former mechanism for water splitting reaction by their Ru-quinone complexes as illustrated in Fig. 2A, where the Ru(II) ion is intact throughout the reaction (25). Similarly Ghosh and Baik (27) have proposed the radical coupling mechanism (A) for the O-O bond formation, though they have considered the contribution of the one-electron transfer from Ru(II) to quinone (**2bb**) as illustrated in Fig. 2B. On the other hand, Muckerman, Fujita and Tanaka et al (25) have considered the superoxide mechanism for water splitting reaction that may be regarded as one of the acid-base (B) mechanism as illustrated in Fig. 2A. However, newly obtained experimental results by Tanaka group (34), together with present DFT computational results may indicate a refined radical coupling mechanism for water splitting reaction as shown in Fig. S7.

The deprotonation of waters in ^{1}**1** in Fig. S7 affords the key tetraradical intermediate ^{1}**3** (^{1}**2bb**) via one-electron transfer (OET) in ^{1}**2**. However, the oxygen-radical pair in ^{1}**3** is local triplet diradical (LTD), suppressing facile O-O bond formation by the radical coupling (RC) mechanism. The two-electron removal from ^{1}**3** provides the hexaradical species ^{3}**4** in Fig. 2 proposed by Ghosh and Baik (27). The oxygen radical pair (see ^{3}A in Fig. S7) is still LTD-type, indicating the necessity of spin inversion (SI) for generation of local singlet diradical (LSD) pair in ^{1}**5** (see ^{1}A in Fig. S4). The RC mechanism in ^{1}**5** is facile, giving the peroxide species ^{1}**6**. The next step for generation of oxygen dianion may become the rate-determining step in the Tanaka catalyst as shown in ^{1}**7**. The b-spin at the terminal oxygen anion in ^{1}**7** is moved to the Ru_2(III) site with the a-spin to form the singlet pair as shown in ^{1}**8**. The spin exchange (SE) between ↓•Ru_1(III) and SQ_1•↑ to generate ↑•Ru_1(III) and SQ_1•↓ is necessary for one more OET from superoxide anion to -•Ru_1(III) to afford triplet molecular oxygen in ^{1}**9**. The SE process is easy because the exchange coupling for the •O-O-Ru(III)• is weak. Thus the SQ_1• radical plays an important role for spin catalysis. The two-electron removal from ^{1}**9** is necessary for reproduction of ^{1}**1**. Thus the BS computational results provide the orbital and spin correlation diagram for water splitting reaction in Fig. S7.

III. 3. Similarity between artificial and native water splitting systems

Very recently Umena, Kawakami, Shen and Kamiya (5) have determined the XRD structure of the OEC of PSII refined to the 1.9 Å resolution, which corresponds to the dark-stable S_1-state of the catalytic cycle (the S_0-S_4 states of the Kok cycle (6)). Their XRD result (5) has elucidated the Mn-Mn, Ca-Mn and Mn-O distances of the $CaMn_4O_5$ cluster and positions of a number of waters in PSII. Very recently possible electronic and spin structures of the $CaMn_4O_5$ cluster (**3**) have been elucidated by the hybrid DFT calculations on the basis of the new X-ray structure (7-10). The DFT computational results provide fundamental information to inspire artificial photosynthesis systems. Thus accumulated experimental and theoretical results (35-44) for OEC of PSII indicated a dual possibility for water splitting reaction: (A) the radical-coupling mechanism and (B) nucleophilic attack of hydroxide anion (water) to the electrophilic metal-oxo species.

The nature of high-valent metal-oxo species is labile as shown in our early paper (45). The high-valent Mn(V)=O bond formally has a triple bond in the sense of the simple MO theory. However, the one ET from HOMO of oxygen dianion to Mn(V) occurs to afford the •Mn(IV)=O•. Moreover, BS solutions for Mn(V)=O indicate continuous variation from the nucleophilic $Mn(V)=O^{2-}$ oxygen to electrophilic oxygen $Mn(III)=O^0$ though •Mn(IV)=O•, depending on electron donating ability of coordination ligands. In fact, oxyl radical character is computationally detected even in the prophyrine Mn(V)=O complex (44). We have thoroughly examined the radical-coupling (RC) mechanism for the O-O bond formation process for the $CaMn_4O_5$ cluster (**3**) in hydrophobic conditions (gas phase) like in the case of the Tanaka catalysts (details are given in Fig. S7). However, the UB3LYP computations have elucidated that the metal diradical character •Mn(IV)=O• of manganese-oxo bond of **3** has been reduced by clustering of waters to active site (46,47). Therefore we have proposed a water-assisted acid-base mechanism in hydrophilic condition (46,47).

Very recent DFT calculations (7-10) also indicated that the orbital overlap for the Mn(IV)-oxyl radical pair of **3** is about 0.5, predicting non-negligible •Mn=O• radical character. This means the oxygen activation by the high-valent Mn ion. However, the orbital overlap at the transition structure (TS) for the O-O bond formation is about 1.0, indicating that the radical character is lost at the TS. Therefore the O-O bond formation between OH and Mn=O is essentially ionic (essentially acid-base type) in nature in accord with the mechanism (B). Recent DFT computations for blue dimmer (22-24,28) also supported the acid-base mechanism under the hydrophilic condition. Fig. S8 illustrates possible analogy between the artificial Ru-quinone complex and the native $CaMn_4O_5$ cluster in OEC of PSII in detail.

Acknowledgment. Computations were carried out using Research Center for Computational

Science, Okazaki, Japan.

References

1. Ferreira K, Iverson T, Maghlaoui K, Baber J, Iwata S Architecture of the Photosynthetic Oxygen-Evolving Center. (2004) *Science* 303; 1831-1838.
2. Loll B, Kern J, Saenger W, Zouni A, Biesiadka J (2005) Towards complete cofactor arrangement in the 3.0Å resolution structure of photosystem II. *Nature* 438: 1040-1044.
3. Robblee JH, Messinger J, Cinco RM, McFarlane KL, Fernandez CC, Pizarro SA, Sauer K, Yachandra VK (2002) The Mn Cluster in the S_0 state of the oxygen-evolving complex of photosystem II studied by EXAFS spectroscopy: are there three di-μ-oxo-bridged Mn_2 moieties in the tetranuclear Mn complex? *J. Am. Chem. Soc.* 124: 7459-7471.
4. Peloguin JM, Britt RD (2001) EPR/ENDOR characterization of the physical and electronic structure of the OEC Mn cluster. *Biochem Biophys Acta* 1503: 96-111.
5. Umena Y, Kawakami K, Shen JR, Kamiya N (2011) Crystal structure of oxygen-evolving photosystem II at a resolution of 1.9Å. *Nature* 473: 55-60.
6. Kok B, Forbush B, McGloin M (1970) Coorperation of charges in photosynthetic O_2 evolution–I. A linear four step mechanism. *Photochem Photobiol* 11: 457-475.
7. Kanda K, Yamanaka S, Saito T, Umena Y, Kawakami K, Shen J–R, Kamiya N, Okumura M, Nakamura H, Yamaguchi K (2011) Labile electronic and spin states of the $CaMn_4O_5$ cluster in the PSII system refined to the 1.9 Å X-ray resolution. UB3LYP computational results. *Chem. Phys. Lett.* 506: 98-103.
8. Saito T, Shoji M, Kanda K, Isobe H, Yamanaka S, Kitagawa Y, Yamada S, Kawakami T, Okumura M, Yamaguchi K (2012) Theory of chemical bonds in metalloenzymes. XVII. Symmetry breaking in manganese cluster structures and chameleonic mechanisms for O–O bond formation of water splitting reaction. *Int. J. Quan.t Chem.* 112: 121-135.
9. Saito T, Yamanaka S, Kanda K, Isobe H, Takano Y, Shigeta Y, Umena Y, Kawakami K, Shen J–R, Kamiya N, Okumura M, Shoji M, Yoshioka Y, Nakamura H, Yamaguchi K (2012) Possible mechanisms of water splitting reaction based on proton and electron release pathways revealed for $CaMn_4O_5$ cluster of PSII refined to 1.9 Å X-Ray resolution. *Int. J. Quant. Chem.* 112: 253-276.
10. Yamanaka S, Saito T, Isobe H, Kanda K, Saito T, Umena Y, Kawakami K, Shen J –R, Kamiya N, Okumura M, Nakamura H, Yamaguchi K (2012) Structure and reactivity of the mixed-valence $CaMn_4O_4(OH)(H_2O)_4$ clusters at oxygen evolution complex of photosystem II. Hybrid DFT (UB3LYP and UBHandHLYP) calculations. *Int. J. Quant. Chem.* 112: 321-343.
11. Wada T, Muckerman JT, Fujita E, Tanaka K (2011) Substituents dependent capability of bis(ruthenium-dioxolene-terpyridine) complexes toward water oxidation. *Dalton Trans.* 40:

2225-2233.

12. Gilbert JA, Eggleston DS, Murphy WR Jr, Geselowwitz DA, Gestrrn SW, Hodgson DJ, Meyer TJ (1985) Structure and redox properties of the water-oxidation catalyst $[(bpy)_2(OH_2)RuORu(OH_2)(bpy)_2]^{4+}$. *J. A. Chem. Soc.* 107: 3855-3864.
13. Llobet A, Curry ME, Evans HT, Meyer TJ (1989) Synthesis, spectral, and redox properties of three triply bridged complexes of ruthenium. *Inorg. Chem.* 28: 3131-3137.
14. Conception J, Jurss JW, Brennaman MK, Hoertz PG, Patrocinio AOT, Iha NYM, Templeton JL, Meyer TJ (2009) Making oxygen with ruthenium complexes. *Accounts Chem. Res.* 42: 1954-1965.
15. Romero I, Rodriquez M, Sens C, Mola J, Kollipara MR, Francas L, Mas-Marza E, Escriche L, Llobet A (2008) Ru complexes that can catalytically oxidize water to molecular dioxygen. *Inorg. Chem.* 47: 1824-1834.
16. Kobayashi K, Ohtsu H, Wada T, Kato T, Tanaka K (2003) Characterization of a stable ruthenium complex with an oxyl radical. *J. Am. Chem. So.c* 125: 6729-6739.
17. Wada T, Yamanaka M, Fujihara T, Miyazato Y, Tanaka K (2006) Experimental and theoretical evaluation of the charge distribution over the ruthenium and dioxolene framework of [Ru(OAc)(dioxolene)(terpy)] (terpy) 2,2′:6′,2′′-terpyridine) depending on the substituents. *Inorg. Chem.* 45: 8887-8894.
18. Kobayashi K, Ohtsu H, Wada T, Tanaka K (2002) Ruthenium oxyl radical complex containing *o*-quinone ligand detected by ESR measurements of spin trapping technique. *Chem. Lett.*: 868-869.
19. Wada T, Tsuge K, Tanaka K (2000) Oxidation of hydrocarbons by mono- and dinuclear ruthenium quinone complexes via hydrogen atom abstraction. *Chem. Lett.*: 910-911.
20. Wada T, Tsuge K, Tanaka K (2000) Electrochemical oxidation of water to dioxygen catalyzed by the oxidized form of the bis(ruthenium–hydroxo) complex in H_2O. *Angew. Chem. Int. Ed.* 39: 1479-1482.
21. Wada T, Tsuge T, Tanaka K (2001) Syntheses and redox properties of bis(hydroxoruthenium) complexes with quinone and bipyridine ligands. Water-Oxidation Catalysis. *Inorg. Chem.* 40: 329-337.
22. Yang X, Baik MH (2004) Electronic structure of the water-oxidation catalyst $[(bpy)_2(OH_x)RuORu(OH_y)(bpy)_2]^{z+}$: Weak coupling between the metal centers is preferred over strong coupling. *J. Am. Chem. Soc.* 126: 13222-13223.
23. Yang X, Baik MH (2006) cis,cis-$[(bpy)2Ru^{V}O]_2O^{4+}$ Catalyzes water oxidation formally via in situ generation of radicaloid Ru^{IV}-O•. *J. Am. Chem. Soc.* 128: 7476-7485.
24. Yang X, Baik MH (2008) The mechanism of water oxidation catalysis promoted by $[tpyRu(IV)–O]_2L^{3+}$: A computational study. *J. Am. Chem. Soc.* 130: 16231-16240.

25. Muckerman JT, Polyansky DE, Wada T, Tanaka K, Fujita E (2008) Water oxidation by a ruthenium complex with noninnocent quinone ligands: possible formation of an O−O bond at a low oxidation state of the metal. *Inorg. Chem.* 47: 1787-1802.

26. Bozoglian F, Romain S, Erterm MZ, Todorova TK, Sens C, Mola J, Rodriguez M, Romero I, Benet-Buchholz J, Fontrodona X, Cramer CJ, Gagliardi L, Llobet A (2009) The Ru-Hbpp water oxidation catalyst. *J. Am. Chem. Soc.* 131: 15176-15187.

27. Ghosh S; Baik MH (2011) Redox properties of Tanaka's water oxidation catalyst: redox noninnocent ligands dominate the electronic structure and reactivity. *Inorg. Chem.* 50: 5946-5957.

28. X. Li, X., Chen G, Schinzel S, Siegbahn REM (2011) A comparison between artificial and natural water oxidation. *Dalton Tran.s* 40: 11296- 11307.

29. Jaque P, Marenich AV, Cramer CJ, Truhlar DG (2007) Computational electrochemistry: the aqueous $Ru^{3+}|Ru^{2+}$ reduction potential. *J. Phys. Chem. C,* 126: 5783-5799.

30. Frish M, J et al, Gaussion, 09 (Gaussian Inc., Wallingford, CT, 2009).

31. Yamaguchi K, F. Jensen, F. , A. Dorigo, A., Houk KN (1988) A spin correction procedure for unrestricted Hartree-Fock and Møller-Plesset wavefunctions for singlet diradicals and polyradicals. *Chem. Phys. Lett.* 149: 537-542.

32. Yamaguchi K, Yamanaka S, Isobe H, Shoji M, Saito T, Kitagawa Y, Okumura M, Shimada J (2009) Theory of chemical bonds in metalloenzymes XIII: singlet and triplet diradical mechanisms of hydroxylations with iron-oxo species and P450 are revisited. *Int. J. Quant. Chem.* 109: 3723-3744.

33. Isobe H, Yamanaka S, Okumura M, Yamaguchi K (2011) Unique structural and electronic features of perferryl–oxo oxidant in cytochrome P450. *J. Phys. Chem. B*, *115*: 10730-10738.

34. Wada T, Tanaka K　Catalytic four-electron oxidation of water via intramolecular coupling of the oxo ligands of bis(ruthenium-bipyridine) complex, *Chem. Eur. J.*: in press.

35. Yano J, Kern J, Sauer K, Latimer MJ, Pushkar Y, Biesiadka J, Loll B, Saenger W, Messinger J, Zouni A, Yachandra VK (2006) Where water is oxidized to dioxygen: structure of the photosynthetic Mn_4Ca cluster. *Science* 314: 821-825.

36. Barber J, Murray JW (2008) QM/MM computational studies of substrate water binding to the oxygen-evolving centre of photosystem II. *Phil. Trans R. Soc.* B, 363: 1149-1156.

37. Petrie S, Stranger R, Pace RJ (2007) Bridge over troubled water: resolving the competing photosystem II crystal structures. *Chem. Eur. J.* 13: 5082-5089,

38. Petrie S, Stranger R, Pace RJ (2008) Structural, magnetic coupling and oxidation state trends in models of the $CaMn_4$ cluster in photosystem II. *Chem. Eur. J.* 14: 5482- 5494.

39. Sproviero EM, Gascon JA, McEvoy JP, Brudvig GW, Batista VS (2006) Characterization of synthetic oxomanganese complexes and the inorganic core of the O_2-evolving complex in

Photosystem II: Evaluation of the DFT/B3LYP level of theory. *J. Inorg. Biochem.* 100: 786-800.

40. Sprovierro EM, Gascon JA, McEvoy JP, Brudvig GW, Batista VSJ (2008) Quantum mechanics/molecular mechanics study of the catalytic cycle of water splitting in photosystem II. *J. Am. Chem. Soc.* 130: 3428- 3442.
41. Zein S, Kulik LV, Yano J, Kern J, Pushkar Y, Zouni A, Yachandra VK, Libitz W, Neese F, Messinger J (2008) Focusing the view on nature's water-splitting catalyst. *Phil. Trans. R. Soc.* B, 363: 1167-1177.
42. Siegbahn PEM (2006) O–O Bond formation in the S_4 state of the oxygen-evolving complex in photosystem II. *Chem. Eur. J.* 12: 9217- 9227.
43. Siegbahn PEM (2009) Structures and energetics for O_2 formation in photosystem II. *Acc. Chem. Res.* 42: 1871- 1880.
44. Yamaguchi K, Shoji M, Saito T, Isobe H, Nishihara S, Koizumi K, Yamada S, Kawakami T, Kitagawa Y, Yamanaka S, Okumura M (2010) Theory of chemical bonds in metalloenzymes. XV. Local singlet and triplet diradical mechanisms for radical coupling reactions in the oxygen evolution complex. *Int. J. Quant. Chem.* 110: 3101-3128.
45. Yamaguchi K, Takahara Y, Fueno T (1986) Ab-initio molecular orbital studies of structure and reactivity of transition metal–oxo compounds. *Appl. Quant. Chem.* (Smith et al, Reidel, 1986): 155-184.
46. Isobe H, Shoji M, Koizumi K, Kitagawa Y, Yamanaka S, Kuramitsu S, Yamaguchi K (2005) Electronic and spin structures of manganese clusters in the photosynthesis II system. *Polyhedron* 24: 2767- 2777.
47. Yamaguchi K, Yamanaka S, Isobe H, Shoji M, Koizumi K, Kitagawa Y, Kawakami T, Okumura M (2007) Theory of chemical bonds in metalloenzymes VI: manganese–oxo bonds in the photosynthesis II system. *Polyhedron* 26: 2216- 2224

Figure Legends

Fig. 1. Possible active intermediates generated by deprotonation (– H^+), oxidation (– e^-) and intramolecular one electron-transfer (OET) of mononuclear ruthenium complex (**1**).

Fig. 2. Possible mechanisms for the oxygen-oxygen (O-O) bond formation by binuclear ruthenium complex (**2**) proposed by Tanaka, Muckerman, Fujita and collaborators (A) and by Ghosh and Baik (B). Muckerman, Fujita and collaborators assume that the divalent Ru(II) ion remains intact throughout the reactions. The radical-coupling and superoxide mechanisms have been proposed for water splitting reaction. Ghosh and Baik assume that the trivalent

Ru(III)-semiquinone (SQ) configuration (**2bb**) plays an important role for water splitting reaction in methanol, while in water solution, an unsymmetrical structure **2a(+)ee** is formed in water solution.

Fig. 3. Possible eight spin structures for four spin-site systems: (abcd) denotes (SQ_2,Ru_2, Ru_1,SQ_1) (**2bb**) or (SQ_2,O_1,Ru_1,SQ_1) (**2a(+)ee)** in accord with the notation for $CaMn_4O_5$ cluster: $CaMn_{a(4)}Mn_{b(3)}Mn_{c(2)}Mn_{d(1)}$(**3**). The same spin Hamiltonian model has been derived to elucidate similarity between artificial (**2bb**) and native (**3**) catalysts for water splitting reaction.

Table Legends

Table 1. Relative energies of **2b**, **2bb**, and **2a(+)ee** at the B3LYP level

Table 2. Effective exchange integrals (J) for the intermediates (**2bb** and **2a(+)ee**)^{a}

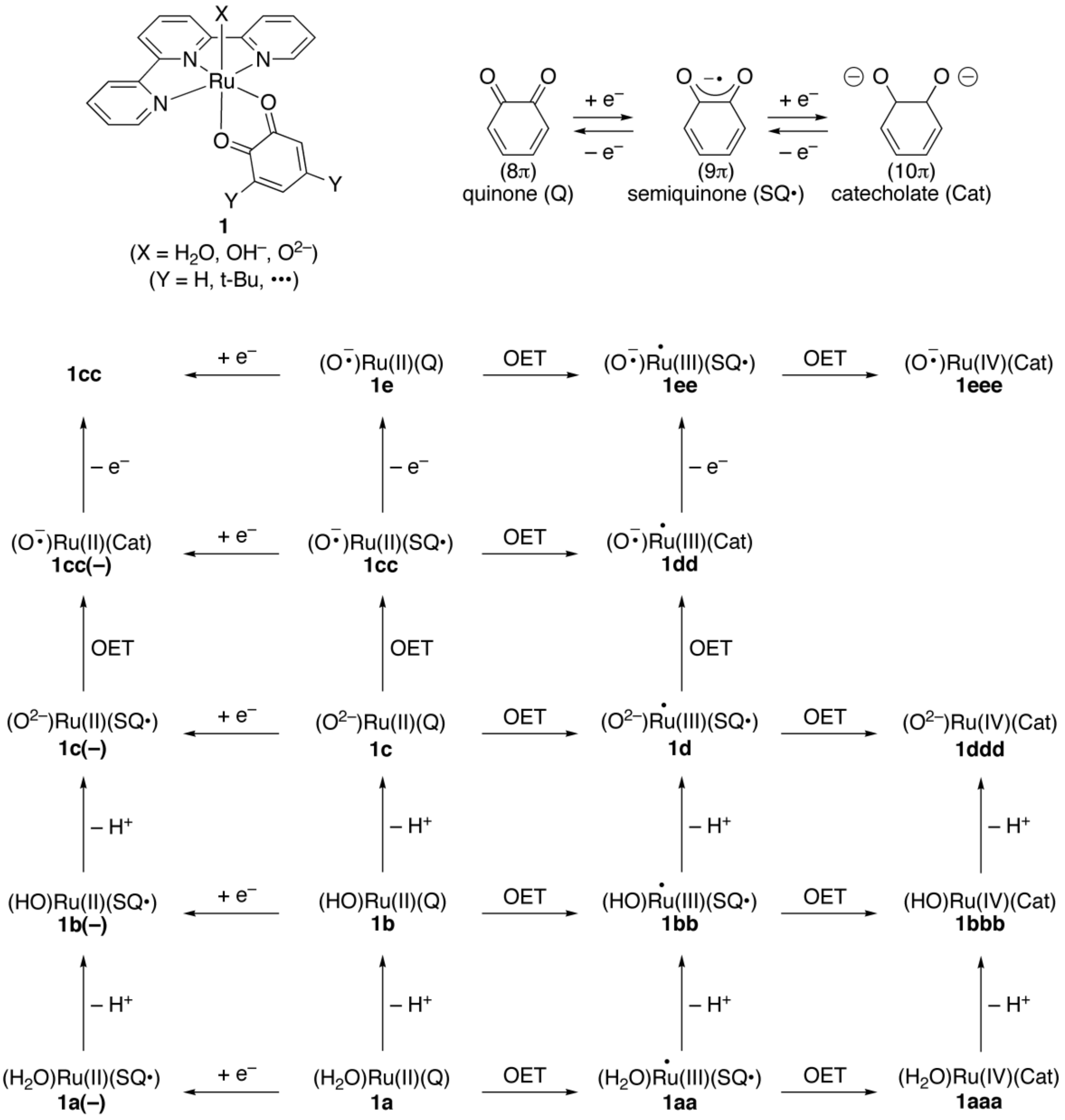

Fig. 1. Possible active intermediates generated by deprotonation (– H^+), oxidation (– e^-) and intramolecular one electron-transfer (OET) of mononuclear ruthenium complex (**1**).

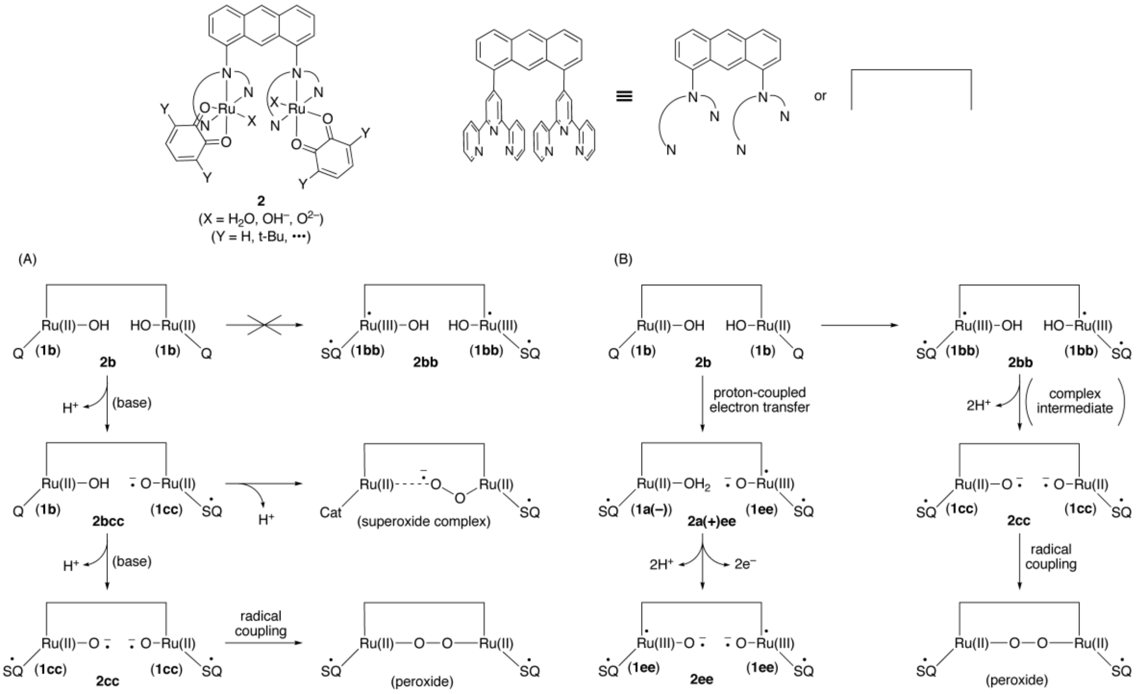

Fig. 2. Possible mechanisms for the oxygen-oxygen (O-O) bond formation by binuclear ruthenium complex (**2**) proposed by Tanaka, Muckerman, Fujita and collaborators (A) and by Ghosh and Baik (B). Muckerman, Fujita and collaborators assume that the divalent Ru(II) ion remains intact throughout the reactions. The radical-coupling and superoxide mechanisms have been proposed for water splitting reaction. Ghosh and Baik assume that the trivalent Ru(III)-semiquinone (SQ) configuration (**2bb**) plays an important role for water splitting reaction in methanol, while in water solution, an unsymmetrical structure **2a(+)ee** is formed in water solution.

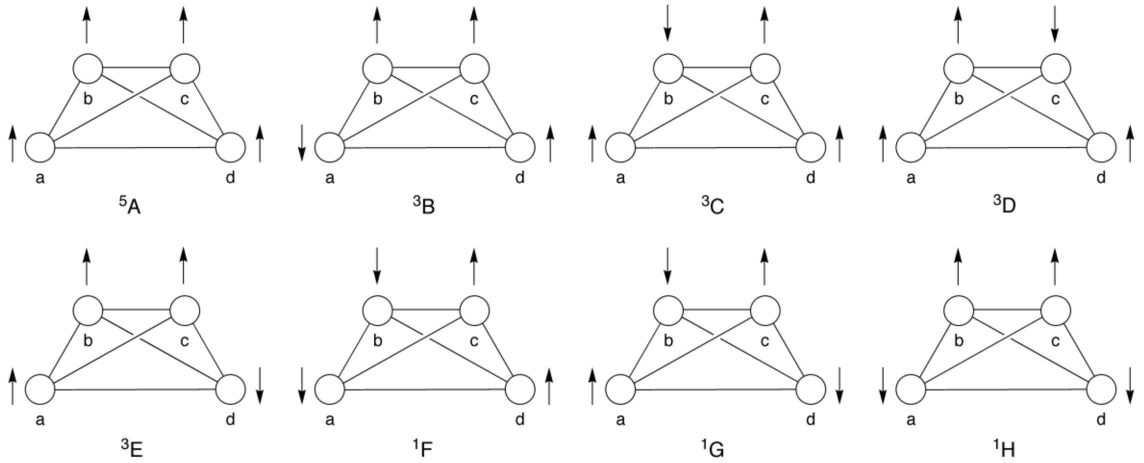

Fig. 3. Possible eight spin structures for four spin-site systems: (abcd) denotes (SQ_2,Ru_2, Ru_1,SQ_1) (**2bb**) or (SQ_2,O_1,Ru_1,SQ_1) (**2a(+)ee)** in accord with the notation for $CaMn_4O_5$ cluster: $CaMn_{a(4)}Mn_{b(3)}Mn_{c(2)}Mn_{d(1)}$(**3**). The same spin Hamiltonian model has been derived to elucidate similarity between artificial (**2bb**) and native (**3**) catalysts for water splitting reaction.

Table 1. Ralative energies of **2b**, **2bb**, and **2a(+)ee** at the B3LYP level

species	spin state	relative energy[a]		$\langle \hat{\mathbf{S}}^2 \rangle$
		before AP	after AP	
2b	CS	0.0 (0.0)[b]	0.0	0.00
2bb	^{5}A	–6.4	–6.4	6.03
	^{3}B	–10.2	–12.2	2.72
	^{3}C	–10.1	–12.1	2.72
	^{3}D	–8.3	–9.6	2.86
	^{3}E	–8.3	–9.7	2.86
	^{1}F	–6.4	–6.4	2.03
	^{1}G	–12.0	–15.4	1.56
	^{1}H	–12.1 (–12.1)[b]	–15.4	1.56
2a(+)ee	^{5}A	–3.1	–3.1	6.03
	^{3}B	–3.1	–3.1	3.03
	^{3}C	3.7	10.1	3.00
	^{3}D	1.0	5.1	2.83
	^{3}E	–5.0	–6.3	2.88
	^{1}F	3.7	10.1	2.00
	^{1}G	1.0	5.2	1.83
	^{1}H	–5.0 (–4.0)[b]	–6.3	1.88

[a] Relative energies without zero-point correction are given in kcal mol^{-1}.

[b] Results by Ghosh and Baik (27) are given in parentheses.

Table 2. Effective exchange integrals (J) for the intermediates (**2bb** and **2a(+)ee**)[a]

J	**2bb**		**2a(+)ee**	
	before AP	after AP	before AP	after AP
J_{ab}	–3.77	–2.89	0.00	0.00
J_{ac}	0.00	0.00	–0.01	–0.01
J_{ad}	–0.01	–0.01	0.00	0.00
J_{bc}	0.03	0.03	6.36	6.13
J_{bd}	–0.01	–0.01	0.42	0.43
J_{cd}	–1.88	–1.61	–2.33	–2.02

[a] J values are given in kcal mol^{-1}.

Similarities of Artificial Photosystems by Ruthenium Oxo Complexes and Native Water Splitting Systems

Supporting Information

I. Theoretical backgrounds

I.1 Charge-transfer diradicals by broken-symmetry calculations

Many donor(D)–acceptor(A) complexes have been investigated by the Mulliken charge-transfer (CT) theory and the closed-shell molecular-orbital (MO) theory as illustrated in Fig. S1A and Fig. S2A. However, the closed-shell singlet configuration (DA) often becomes unstable than the open-shell one-electron transfer (ET) triplet configuration (•+DA–•) as illustrated in Fig. S2B (45, S1, S2). The closed-shell picture breaks down for open-shell systems (•+DA-•). Nowadays spin-polarized hybrid DFT (HDFT) calculations have been extensively performed for open-shell systems generated by electron transfer reactions. In fact, the broken symmetry computational methods based on a single Slater determinant model provide molecular orbitals (MO) concepts that are useful and handy for lucid understanding of labile chemical bonds consisted of the donor and acceptor sites. The energy gap between DA and -•+DA-•¯ configurations is approximately given by (45, S1, S2)

$$\lambda = \varepsilon(LUMO(A)) - \varepsilon(HOMO(D)) - U(HOMO(D)), \qquad \text{(S1a)}$$

where $\varepsilon(LUMO(A))$ and $\varepsilon(HOMO(D))$ denote, respectively, orbital energies of LUMO of A and HOMO of D, and $U(HOMO(D))$ is the on-site repulsion integral for the electron pair at HOMO(D). The closed-shell singlet configuration becomes unstable for fluctuation of the triplet excitation if λ-value is negative in sign, reorganized into a more stable open-shell one-ET singlet configuration in Fig. S1C(D) (S1, S2). In fact, the broken-symmetry MOs are expressed by the HOMO-LUMO mixing of electron donor site (D) and electron acceptor site (A) if $\lambda < 0$ as

$$\psi^{+} = \cos\theta_1\phi_{HOMO(D)} + \sin\theta_1\phi^{*}_{LUMO(A)} \qquad \text{(S2a)}$$

$$\psi^{-} = \cos\theta_2\phi^{*}_{LUMO(A)} + \sin\theta_2\phi_{HOMO(D)} \qquad \text{(S2b)}$$

where θ_1 and θ_2 denote the orbital mixing parameters determined by the SCF calculations of hybrid UDFT. $\phi_{HOMO(D)}$ and $\phi^{*}_{LUMO(A)}$ denote, respectively, the highest-occupied MO of electron donor (D) and lowest-unoccupied MO of acceptor (A), respectively (see Fig. S1).

The BS solutions in eq. S2 appears if the HOMO(D)-LUMO(A) gap becomes small. This implies that the electronegativity or Coulomb integral (α) of D and A sites play an important role for strong CT interaction. As shown in previous Hückel-Hubbard Hamiltonian (HH), the orbital mixing parameters (45, S1, S2) are dependent on the ionicity (y) and covalent bonding (x) parameters defined by

$$y = \varepsilon(LUMO(A)) - \varepsilon(HOMO(D)) / U(HOMO(D)) \qquad \text{(S3c)}$$

$$x = -\beta(LUMO(A)) \mid \varepsilon(HOMO(D)) / U(HOMO(D)), \qquad \text{(S3d)}$$

where $\beta(LUMO(A)) \mid \varepsilon(HOMO(D))$ denotes the resonance integral between HOMO(D) and LUMO(A). The total energy and orbital mixing parameters in eq. S2 are expressed by functions of the x- and y-parameters in the HH model.

The orbital overlap T between BS MOs in eq. S2 is introduced to express localizability of broken-symmetry orbitals. It is defined as

$$T = <\Psi^{+} \mid \Psi^{-}> = \cos\theta_1 \sin\theta_2 + \sin\theta_1 \cos\theta_2 . \qquad \text{(S4)}$$

The orbital overlap T becomes 1.0 in the case of the closed-shell case; $\psi^{+} = \psi^{-} = \phi_{HOMO(D)}$ (θ_1 = 0 and θ_2 = $\pi/2$). This means that BS MOs reduce to the closed-shell HOMO(D) pair because of the large HOMO(D)-LUMO(A) gap as illustrated in Fig. S1A, showing no charge-transfer diradical character. The closed-shell MO pictures (T_i = 1.0) accompanied with no radical character are already used for beautiful explanation of stable organometallic cluster compounds. On the other hand, the orbital overlap T also becomes 1.0 in the case of the other closed-shell case; $\psi^{+} = \psi^{-} = \phi^{*}_{LUMO(A)}$ (θ_1= $\pi/2$ and θ_2 = 0). BS MOs reduce to the closed-shell LUMO(A) pair because of the large negative HOMO(D)-LUMO(A) gap as illustrated in Fig. S1B, indicating the two-electron (electron pair) transfer: note that the HOMO(D)-LUMO(A) gap is still positive in Fig. S1B. However, the large on-site repulsion integral ($U(HOMO(D))$ at a donor site (for example Ru(II)) exceeds the orbital energy gap in a strongly correlated electron system (large U in the HH model).

The orbital overlap T is 0.0 for a special case (θ_1 = θ_2 = 0), where $\psi^{+} = \phi_{HOMO(D)}$ and $\psi^{-} = \phi^{*}_{LUMO(A)}$. This corresponds to the pure one-electron (ET) transfer diradical state -•+DA-•‾: a down-spin electron is transferred from HOMO(D) to LUMO(A) as illustrated in Fig. S1C. The orbital overlap T also becomes 0.0 for the other special case (θ_1 = θ_2 = $\pi/2$), where $\psi^{+} = \phi^{*}_{LUMO(A)}$ and $\psi^{-} = \phi^{*}_{HOMO(D)}$. This means that an up-spin electron is transferred from HOMO(D) to LUMO(A), giving the pure one-electron (ET) transfer diradical configuration ¯•+DA-•- in Fig. S1D. Thus the broken-symmetry orbitals provide the MO-theoretical description of no ET (G), one-electron (ET) transfers or two-electron (double (D) ET (DET)) configuration. Moreover they can describe partial electron-transfer states that are mixing of the ground (G), pure ET and DET configurations in general (45, S1, S2).

I.2 Configuration interaction explanation of BS solution

In order to obtain the configuration interaction (CI) picture, BS solutions are expanded using the ground, one-electron transfer (OET) and double ET (DET) configurations. The BS MO configuration can be indeed expanded by using HOMO(D) and LUMO(A) to describe the configuration mixing state as

$$\Psi_{BSI} = |\,\psi^{+}(\alpha)\psi^{-}(\beta)\,| \tag{S5a}$$

$$= |\,(\cos\theta_1\phi_{HOMO(D)} + \sin\theta_1\phi^{*}_{LUMO(A)})(\alpha)(\cos\theta_2\phi^{*}_{LUMO(A)} + \sin\theta_2\phi_{HOMO(D)})(\beta)\,| \tag{S5b}$$

$$= \cos\theta_1\sin\theta_2\Phi_G + \cos\theta_2\sin\theta_1\sin\theta_1\Phi_{DET} + \cos(\theta_1-\theta_2)\Phi_{ET(S)} + \cos(\theta_1+\theta_2)\Phi_{ET(T)}, \tag{S5c}$$

where the pure singlet (SD) and triplet (TD) ET states are given by two configurations.

$$\Phi_{ET(S)} = (|\,\phi_{HOMO(D)}(\alpha)\phi^{*}_{LUMO(A)}(\beta)\,| + |\,\phi^{*}_{LUMO(A)}(\alpha)\phi_{HOMO(D)}(\beta)\,|)/\sqrt{2} \tag{S6a}$$

$$\Phi_{ET(T)} = (|\,\phi_{HOMO(D)}(\alpha)\phi^{*}_{LUMO(A)}(\beta)\,| - |\,\phi^{*}_{LUMO(A)}(\alpha)\phi_{HOMO(D)}(\beta)\,|)/\sqrt{2} \tag{S6b}$$

On the other hand, the ground (G) and double ET (DET) states are given by the closed-shell configuration.

$$\Phi_G = |\,\phi_{HOMO(D)}(\alpha)\phi_{HOMO(D)}(\beta)\,|, \Phi_{DET} = |\,\phi^{*}_{LUMO(A)}(\alpha)\phi^{*}_{LUMO(A)}(\beta)\,| \tag{S7}$$

The low-spin (LS) BSI MO configuration involves both singlet one ET diradical (+•D-A-•) and double ET (DET(++D-A--) configuration as in the case of the configuration interaction (CI) scheme, but it also includes the pure triplet ET DR (TD) component, showing the spin-symmetry breaking property. Similarly, the low-spin (LS) BSII MO configuration is expressed by

$$\Psi_{BSI} = |\,\psi^{-}(\alpha)\psi^{+}(\beta)\,| \tag{S8a}$$

$$= |\,(\cos\theta_2\phi^{*}_{LUMO(A)} + \sin\theta_2\phi_{HOMO(D)})(\alpha)(\cos\theta_1\phi_{HOMO(D)} + \sin\theta_1\phi^{*}_{LUMO(A)})(\beta)\,| \tag{S8b}$$

$$= \cos\theta_1\sin\theta_2\Phi_G + \cos\theta_2\sin\theta_1\sin\theta_1\Phi_{DET} + \cos(\theta_1-\theta_2)\Phi_{ET(S)} - \cos(\theta_1+\theta_2)\Phi_{ET(T)} \tag{S8c}$$

The LS BSII MO solution also involves both singlet one ET diradical (+•D-A-•) and double ET (DET(++D-A--) configuration, but it also includes the pure triplet ET DR (TD) component. Thus the spin symmetry breaking is inevitable for ET diradical species in the case of the single-determinant (reference) BS solution; the Hartree-Fock and Kohn-Sham DFT models belong to this category. Nevertheless, BS methods can be regarded as a convenient and handy procedure to determine both delocalized and localized MOs for open-shell transition-metal clusters such as **1**, **2**, and **3**. On the other hand, both orbital and spin symmetries should be conserved in finite systems such as **1**, **2**, and **3** (45, S1, S2). Then the recovery of them is performed for quantitative purpose as shown below (31, 45, S3, S4).

I. 3 Recovery of spin symmetry via quantum resonance

The recovery of broken spin symmetry in the BSI and BSII solutions is crucial for derivation of the pure singlet and triplet states. In fact, the quantum resonance of them is feasible because of the energy degeneracy between BSI and BSII as follows (S3, S4):

$$\Phi_{RBS(+)} = (\Psi_{BSI} + \Psi_{BSII}) / \sqrt{2} \tag{S9a}$$

$$= (\cos\theta_1 \sin\theta_2 \Phi_G + \cos\theta_2 \sin\theta_1 \sin\theta_1 \Phi_{DET} + \cos(\theta_1 - \theta_2)\Phi_{ET(S)})N \tag{S9b}$$

$$\Phi_{RBS(-)} = (\Psi_{BSI} - \Psi_{BSII}) / \sqrt{2} \tag{S10a}$$

$$= \Phi_{ET(T)}, \tag{S10b}$$

where N denotes the normalizing factor. Thus the in- and out-of-phase resonating BS (RBS) solutions are nothing but the pure singlet and triplet states wave functions, respectively. The chemical bonding between donor and acceptor sites is expressed with the mixing of the ground singlet (G), singlet ET diradical and double ET (DET) configurations under the resonating BS (RBS) approximation. The CI type explanation of electronic structures becomes feasible under the RBS approximation as illustrated in Fig. S2. The degenerated BS solutions split into the pure singlet and triplet states, and their energy gap is given by 2J where J means the effective exchange integrals in the Heisenberg model for diradical species. J value is defined by the total energies (E) of the singlet and triplet biradicals 2J = E(S) – E(T). Therefore the singlet ET state becomes more stable than the triplet ET state if the J value is negative (antiferromagnetic) as shown in Fig. S2B. The situation is reversed if J is positive (ferromagnetic) as illustrated in Fig. S2C.

I.4 Charge and spin densities by broken-symmetry solutions

The spin densities appear under the BS approximation even in the antiferromagnetic (AF) low-spin (LS) singlet-type BS configuration, though they should disappear in the exact singlet state in eq. S9. In fact, the charge density $P_1(\mathbf{r}_1,\mathbf{r}_1)$ and spin density $Q(\mathbf{r}_1,\mathbf{r}_1)$ are given by the broken-symmetry (BS) orbitals in eq. S2 as follows (S5-S7)

$$P_1(r,r) = (\psi^+)^2 + (\psi^+)^2 \tag{S11a}$$

$$= (\cos^2\theta_1 + \sin^2\theta_2)\phi^2{}_{HOMO(D)} + (\sin^2\theta_1 + \cos^2\theta_2)\phi^2{}_{LUMO(A)} \tag{S11b}$$

$$Q(r,r) = (\psi^+)^2 - (\psi^+)^2 \tag{S12a}$$

$$= (\cos^2\theta_1 - \sin^2\theta_2)\phi^2{}_{HOMO(D)} + (\sin^2\theta_1 \text{-} \cos^2\theta_2)\phi^2{}_{LUMO(A)} \tag{S12b}$$

The spin density disappears at the closed-shell limits: (A) $\theta_1 = 0$ and $\theta_2 = \pi/2$ and (B) $\theta_1 = \pi/2$ and $\theta_2 = 0$. The cases (A) and (B) correspond to the ground (G) and double ET (DET) states in Figs. S1A(2A) and S1B, respectively. Therefore the populations of charge density in eq. 11 are 2 on the HOMO(D) and on the LUMO(A), respectively, for these states. On the other hand, the populations of spin density becomes 1 on HOMO(D) and -1 on LUMO(A), respectively, in the case of one ET DR configuration (C) $\theta_1 = \theta_2 = 0$ in Fig. S1C, whereas they are -1 on HOMO(D) and 1 on LUMO(A), respectively, in the case of one ET DR configuration (D) $\theta_1 = \theta_2 = \pi/2$ in Fig. S1D. On the other hand, weight of one ET DR configuration can be estimated by population of spin density on the donor (D+•) and/or acceptor (A-•) site. Thus charge and spin populations by the BS solutions are handy and useful for qualitative understanding of diradical configurations.

In early 1970s the spin-symmetry breaking is an origin of serious critics for BS approach by Löwdin. This enabled one of the authors (KY) to consider a basic question regarding what is the spin density in the LS BS solution; only spin contamination errors? Therefore physical basis of appearance of the spin density should be clarified in the case of AF LS BS solutions. Indeed, important roles of spin densities emerge via the analysis of pair and spin correlation functions of the BS solutions as shown in our previous papers (S5-S8). The on-site pair function (P_2) for electrons with different spins is given by

$$P_2(\mathbf{r}_1,\mathbf{r}_1;\mathbf{r}_1,\mathbf{r}_1) = \left[P_1(\mathbf{r}_1,\mathbf{r}_1)^2 - Q(\mathbf{r}_1,\mathbf{r}_1)^2\right]/2, \tag{S13}$$

where $P_1(\mathbf{r}_1,\mathbf{r}_1)^2$ and $Q_1(\mathbf{r}_1,\mathbf{r}_1)^2$ denotes, respectively, the density and spin density. P_2 directly expresses the Coulomb repulsion $P_2\, U(HOMO(D))$ between electrons with opposite spins. This means that the magnitude of spin density is parallel to the size of

Coulomb hole for electrons with different spins. Then the unpaired electron density U responsible for deviation from the single determinant is expressed by the square of spin density under the BS approximation (S5-S7) as

$$U(\mathbf{r}_1) = Q(\mathbf{r}_1, \mathbf{r}_1)^2 = Q(\mathbf{r}_1)^2. \qquad \text{(S14a)}$$

The magnitude of spin densities reported in various recent BS calculations can be understood from the view point of nondynamical correlations between electrons with different spins, namely strong electron repulsion effects. Therefore the spin density index is also introduced to express the characteristic behavior of the spin density as

$$Q\ (\mathbf{r}_1, \mathbf{r}_1) = \sqrt{U\ (r)} = \sqrt{1 - T^2} \qquad \text{(S14b)}$$

On the other hand, determination the sign of spin densities is a basic problem under the BS approximation. In order to elucidate this problem, the spin correlation function that is directly related to the Penney's bond order is introduced since it can be observed in the case of infinite systems with neutron diffraction technique. In fact, the spin correlation function $K_2(\mathbf{r}_1, \mathbf{r}_2)$ is approximately given by

$$K_2(\mathbf{r}_1, \mathbf{r}_2) = \int \mathbf{S}(1) \cdot \mathbf{S}(2) P_2(\mathbf{r}_1, \mathbf{r}_2; \mathbf{r}_1, \mathbf{r}_2) \mathrm{ds} \qquad \text{(S15a)}$$

$$\approx Q(\mathbf{r}_1) Q(\mathbf{r}_2). \qquad \text{(S15b)}$$

where $P_2(\mathbf{r}_1, \mathbf{r}_2; \mathbf{r}_1, \mathbf{r}_2)$ denotes the second-order density matrix. This means that the spin correlation is singlet-type if the sign of spin density product is negative; (↑↓) or (↓↑) (see also Fig. 1C and 1D). In this paper, we have used such a pictorial expression of the antiferromagetic (AF) low-spin (LS) singlet state. The sign of spin density is closely related to the spin correlation function under the BS approximation. Although the spin densities arising from the first-order density $P_1(\mathbf{r}_1, \mathbf{r}_2)$ disappears at the pure singlet state, the unpaired electron density (U) and spin correlation function (K_2) still exist as important electron and spin correlation indices even in the resonating BS (RBS). Therefore sign and magnitude of spin densities in Table 3 (see below) in this article should be understood from the above theoretical viewpoints. The pair and spin correlation functions can be used to elucidate the nature of chemical bonds in the case of RBS and multi-reference (MR) approaches as alternative indices for spin density at the hybrid density functional (HDFT) (for example BS UB3LYP) level of theory.

I.5 Noncollinear spin structures described by general spin orbitals (GSO)

The up and down spin orbitals in eq. S2 are often mixed into general spin orbitals (GSO) to express noncollinear spin structures (44,46,S6,S7,S9-S11) responsible for spin frustration effects in triangular and cubane-type clusters such as $CaMn_4O_5$.

$$\psi^{GSO} = \cos\omega\ \psi^{+}\alpha + \sin\omega\ \psi^{-}\beta \qquad \text{(S2c)}$$

where w means the mixing parameter of the up and down spin components. The spin density matrix obtained by the GSO DFT has the non-zero off-diagonal parts that provide the three-dimensional (3D) spin densities : $Q=(Q_x,Q_y,Q_z)$. Therefore the spin density is expressed by 3D spin vector. On the other hand, the one-dimensional spin density: $Q=(0,0,Q_z)$ is expressed by the collinear spin structure. GSO DFT calculations of cubane-type Mn_4 clusters provided the tetrahedral spin structure as shown in refs. 46.

The non-nearest neighbor effective exchange integrals (Jac, Jad, Jbc) for Tanaka catalyst are small as shown in Table 2 (see text), as compared with the nearest neighbor effective exchange integrals (Jab, Jbc, Jcd). This means the distortions of spins by the former exchange integrals, namely spin frustration effects, are weak, providing the collinear spin structures as shown in Fig. 3.

I.6 Scope and applicability of BS DFT methods revealed by MkMRCC

Scope and applicability of broken-symmetry (BS) hybrid DFT methods for theoretical calculations of J values in the Heisenberg model have been examined by comparison with the corresponding J values obtained by symmetry-adapted (SA) Mukerjii-type (Mk) multi-reference (MR) coupled-cluster (CC) methods. The MkMRCC results for typical biradical species have indicated that BS DFT methods such as UB3LYP are reliable enough for semi-quantitave calculations of J values of the species (S12,S13).

References

S1. Takabe T, Yamaguchi K (1976) Electron-transfer biradical intermediates in ground-state reactions. *Chem Phys Lett* 40:347-352.

S2. Takabe T, Takenaka K, Yamaguchi K, Fueno T (1976) On the mechanisms of aromatic substitution reactions. *Chem Phys Lett* 44:65-69.

S3. Nishihara S, Yamanaka S, Kusakabe K, Nakata K, Yonezawa Y, Nakamura H, Yamaguchi K (2009) A resonating broken symmetry configuration interaction approach for double-exchange magnetic systems. *J Phys Condens Matter* 21:064227 (5pages).

S4. Yamanaka S, Nishihara S, Nakata K, Yonezawa Y, Okumura M, Takada T, Nakamura H, Yamaguchi K (2009) Resonating coupled-cluster CI approach to ion-radical systems: comparison with the unrestricted coupled-cluster approach. *Int J Quant Chem* 109:3811- 3818.

S5. Yamaguchi, K, Fueno, T (1977) Correlation effects in singlet biradical species. *Chem Phys* 19:35-42.

S6. Yamaguchi, K (1978) Generalized molecular orbital (GMO) theories of organic reaction mechanisms. Orbital symmetry, orbital stability and orbital pairing rules

Chem Phys 29:117-139.

S7. Yamaguchi, K (1990) Instability in chemical bonds. SCF, APUMP, APUCC, MR-CI and MR-CC approaches. Self-Consistent Field, Theory and Applications (R. Carbo and M. Klobukowski, Elsevier, 1990): 727-823.

S8. Yamaguchi, K, Fueno, T (1977) Diradical and zwitterionic intermediates in the excited state. *Chem Phys* 23:375-386.

S9. Yamaguchi, K (1975) General spin structures of organic radicals. *Chem. Phys. Lett*. 30: 288-291.

S10. Yamaguchi, K, Fueno, T, Ozaki, M, Ueyama, N, Nakamura. A (1990) General spin orbital (GSO) description of antiferromagnetic spin coupling between four irons in iron-sulfur clusters. *Chem. Phys. Lett*. 168: 56-62.

S11. Yamaguchi, K, Yamanaka, S, Nishino, M, Takano, Y, Kitagawa, Y, Nagao, H, Yoshioka, Y (1999) Symmetry and broken symmetries in molecular orbital descriptions of unstable molecules II. Alignment, frustration and tunneling of spins in mesoscopic molecular magnets. *Theor. Chem. Acc.* 102: 328-345.

S12. Nishihara, S, Saito, T, Yamanaka, S, Kitagawa, Y, Kawakami, T, Okumura, M, Yamaguchi, K (2010) MkMRCC, APUCC and APUBD approaches to 1,n-di-dehydropolyene diradicals: the nature of through-bond exchange interactions. *Mol. Phys.* 108: 2559-2578.

S13. Saito, T, Yasuda, N, Nishihara, S, Yamanaka, S, Kitagawa, Y, Kawakami, T, Okumura, M, Yamaguchi, K (2011) Broken-symmetry natural orbital (BSNO)-Mk-MRCC study on the exchange coupling in the binuclear copper (II) compounds. *Chem. Phys. Lett*. 505: 11-15.

II. Heisenberg spin Hamiltonian model and classical approximation

Magnetic measurements have been performed for a number of exchange-coupled systems. The Heisenberg spin Hamiltonian model has been employed for the analysis of experimental results available. In order to elucidate similarity between the Tanaka catalyst **2** and $CaMn_4O_5$ (**3**), we here consider the model Hamiltonian for four-site four-spin systems like **2bb** and **2a(-)ee**. Heisenberg spin Hamiltonian for the systems is given by (7-10)

$$\begin{aligned}
\mathbf{H} &= -2J_{ab}\mathbf{S}_a \cdot \mathbf{S}_b - 2J_{ac}\mathbf{S}_a \cdot \mathbf{S}_c - 2J_{ad}\mathbf{S}_a \cdot \mathbf{S}_d - 2J_{bc}\mathbf{S}_b \cdot \mathbf{S}_c - 2J_{bd}\mathbf{S}_b \cdot \mathbf{S}_d - 2J_{cd}\mathbf{S}_c \cdot \mathbf{S}_d \\
&= -J_{ab}[(\mathbf{S}_a + \mathbf{S}_b)^2 - \mathbf{S}_a{}^2 - \mathbf{S}_b{}^2] - J_{ac}[(\mathbf{S}_a + \mathbf{S}_c)^2 - \mathbf{S}_a{}^2 - \mathbf{S}_c{}^2] - J_{ad}[(\mathbf{S}_a + \mathbf{S}_d)^2 - \mathbf{S}_a{}^2 - \mathbf{S}_d{}^2] \\
&\quad -J_{bc}[(\mathbf{S}_b + \mathbf{S}_c)^2 - \mathbf{S}_b{}^2 - \mathbf{S}_c{}^2] - J_{bd}[(\mathbf{S}_b + \mathbf{S}_d)^2 - \mathbf{S}_b{}^2 - \mathbf{S}_d{}^2] - J_{cd}[(\mathbf{S}_c + \mathbf{S}_d)^2 - \mathbf{S}_c{}^2 - \mathbf{S}_d{}^2] \\
&= -J_{ab}\mathbf{S}_{ab}{}^2 - J_{ac}\mathbf{S}_{ac}{}^2 - J_{ad}\mathbf{S}_{ad}{}^2 - J_{bc}\mathbf{S}_{bc}{}^2 - J_{bd}\mathbf{S}_{bd}{}^2 - J_{cd}\mathbf{S}_{cd}{}^2 \\
&\quad +\mathbf{S}_a{}^2(J_{ab} + J_{ac} + J_{ad}) + \mathbf{S}_b{}^2(J_{ab} + J_{bc} + J_{bd}) + \mathbf{S}_c{}^2(J_{bc} + J_{cd} + J_{ac}) + \mathbf{S}_d{}^2(J_{cd} + J_{ad} + J_{bd})
\end{aligned}$$

(S16)

where $\mathbf{S}_i$ means the spin operator, and the sum of the spin operators is defined by

$$\mathbf{S}_{ij} = \mathbf{S}_i + \mathbf{S}_j, \mathbf{S}_i = local\ spin\ on\ Ru\ and\ quinone \qquad \text{(S17)}$$

Therefore the expectation value for the spin Hamiltonian is given on the quantum mechanics as

$$\begin{aligned}
<\mathbf{H}>_Q = &-J_{ab}S_{ab}(S_{ab}+1) \ - J_{ac}S_{ac}(S_{ac}+1) \ - J_{ad}S_{ad}(S_{ad}+1) \\
&-J_{bc}S_{bc}(S_{bc}+1) \ - J_{bd}{}^2S_{bd}(S_{bd}+1) \ - J_{cd}S_{cd}(S_{cd}+1) \\
&+S_a(S_a+1)(J_{ab}+J_{ac}+J_{ad}) + S_b(S_b+1)(J_{ab}+J_{bc}+J_{bd}) \\
&+S_c(S_c+1)(J_{bc}+J_{cd}+J_{ac}) + S_d(S_d+1)(J_{cd}+J_{ad}+J_{bd})
\end{aligned}, \qquad \text{(S18)}$$

where S_i and S_{ij} are spin quantum numbers of quantum spin i and spin pair (ij) in eq. (S17), respectively. J_{ab} denotes the effective exchange integral between sites a and b that is given by the average of orbital contributions i and j. J_{ab} values can be determined by the electron spin resonance (ESR) and other magnetic measurements.

The expectation values of the Heisenberg spin Hamiltonian are often approximated on the assumption that local spins are regarded as classical (axial) spin (vector). Here the up- and down-spin vectors are considered in accord with broken-symmetry calculations of the different-orbitals-for-different-spins (DODS) type. Then the expectation values of the classical Heisenberg model are given by

$$\begin{aligned}
<\mathbf{H}>_C = &-J_{ab}S_{ab}{}^2 - J_{ac}S_{ac}{}^2 - J_{ad}S_{ad}{}^2 \ - J_{bc}S_{bc}{}^2 - J_{bd}{}^2S_{bd}{}^2 - J_{cd}S_{cd}{}^2 \\
&+S_a{}^2(J_{ab}+J_{ac}+J_{ad}) + S_b{}^2(J_{ab}+J_{bc}+J_{bd}) \\
&+S_c{}^2(J_{bc}+J_{cd}+J_{ac}) + (J_{cd}+J_{ad}+J_{bd})
\end{aligned} \qquad \text{(S19)}$$

Fig. 3 illustrates possible spin alignments of four spin vectors in **2bb**. The energy expressions for eight spin alignments in Fig. 3 are explicitly given under the classical approximation as

$$
\begin{aligned}
&{}^{5}< \mathbf{H} >_{A} = -J_{ab} - J_{ac} - J_{ad} - J_{bc} - J_{bd} - J_{cd} \\
&{}^{3}< \mathbf{H} >_{B} = -J_{bc} - J_{bd} \; - J_{cd} \\
&{}^{3}< \mathbf{H} >_{C} = -J_{ac} - J_{ad} - J_{cd} \\
&{}^{3}< \mathbf{H} >_{D} = -J_{ab} - J_{ad} - J_{bd} \\
&{}^{3}< \mathbf{H} >_{E} = -J_{ab} - J_{ac} - J_{bc} \\
&{}^{1}< \mathbf{H} >_{F} = -J_{ab} - J_{cd} \\
&{}^{1}< \mathbf{H} >_{G} = -J_{ac} - J_{bd} \\
&{}^{1}< \mathbf{H} >_{H} = -J_{ad} - J_{bc}
\end{aligned}
\tag{S20}
$$

where the constant terms are abbreviated for simplicity.

The total energies of the classical Heisenberg model correspond, respectively, to those of eight BS solutions. The energy gaps are calculated by setting the total energy of the AF singlet configuration (^{1}G) as the reference.

$$
\begin{aligned}
&{}^{5}\Delta < \mathbf{H} >_{A} = -J_{ab} - J_{ad} - J_{bc} - J_{cd} = 5.667 \\
&{}^{3}\Delta < \mathbf{H} >_{B} = -J_{bc} - J_{cd} \; + J_{ac} = 1.843 \\
&{}^{3}\Delta < \mathbf{H} >_{C} = -J_{cd} - J_{ad} + J_{bd} = 1.877 \\
&{}^{3}\Delta < \mathbf{H} >_{D} = -J_{ab} - J_{ad} + J_{ac} \; = 3.773 \\
&{}^{3}\Delta < \mathbf{H} >_{E} = -J_{ab} - J_{bc} + J_{bd} = 3.725 \\
&{}^{1}\Delta < \mathbf{H} >_{F} = -J_{ab} - J_{cd} + J_{ac} + J_{bd} \\
&{}^{1}\Delta < \mathbf{H} >_{H} = -J_{ad} - J_{bc} + J_{ac} + J_{bd} = -0.035
\end{aligned}
\tag{S21a}
$$

These equations are utilized for computations of J values under the classical approximation.

$$
\begin{aligned}
&J_{ab} = ({}^{1}\Delta < \mathbf{H} >_{H} - {}^{3}\Delta < \mathbf{H} >_{D} - {}^{3}\Delta < \mathbf{H} >_{E}) / 2 = -3.77(-2.89) \\
&J_{ac} = ({}^{3}\Delta < \mathbf{H} >_{D} + {}^{3}\Delta < \mathbf{H} >_{B} - {}^{5}\Delta < \mathbf{H} >_{A}) / 2 = -0.00(0.00) \\
&J_{ad} = ({}^{3}\Delta < \mathbf{H} >_{E} + {}^{3}\Delta < \mathbf{H} >_{B} - {}^{1}\Delta < \mathbf{H} >_{H} - {}^{5}\Delta < \mathbf{H} >_{A}) / 2 = -0.01(0.01) \\
&J_{bc} = ({}^{3}\Delta < \mathbf{H} >_{D} + {}^{3}\Delta < \mathbf{H} >_{C} - {}^{1}\Delta < \mathbf{H} >_{H} - {}^{5}\Delta < \mathbf{H} >_{A}) / 2 = 0.03(0.03) \\
&J_{bd} = ({}^{3}\Delta < \mathbf{H} >_{C} + {}^{3}\Delta < \mathbf{H} >_{E} - {}^{5}\Delta < \mathbf{H} >_{A}) / 2 = -0.01 \\
&J_{cd} = ({}^{1}\Delta < \mathbf{H} >_{H} - {}^{3}\Delta < \mathbf{H} >_{B} - {}^{3}\Delta < \mathbf{H} >_{C}) / 2 = -1.88(-1.61)
\end{aligned}
\tag{S22a}
$$

As expected energy levels in section II.1, Jab and Jcd are negative in sign, indicating the greater stability of the singlet pairs. However, the magnitude is considerably different in accord with the unsymmetrical electronic state as shown below.

The energy gaps for the eight spin configurations for **2a(+)ee** are calculated by setting the total energy of the AF singlet configuration (^{1}G) as the reference.

$$\begin{aligned}
{}^{5}\Delta < \mathbf{H} >_{A} &= -J_{ab} - J_{ad} - J_{bc} - J_{cd} = -4.028 \\
{}^{3}\Delta < \mathbf{H} >_{B} &= -J_{bc} - J_{cd} + J_{ac} = -4.035 \\
{}^{3}\Delta < \mathbf{H} >_{C} &= -J_{cd} - J_{ad} + J_{bd} = 2.753 \\
{}^{3}\Delta < \mathbf{H} >_{D} &= -J_{ab} - J_{ad} + J_{ac} = -0.01 \\
{}^{3}\Delta < \mathbf{H} >_{E} &= -J_{ab} - J_{bc} + J_{bd} = -5.939 \\
{}^{1}\Delta < \mathbf{H} >_{F} &= -J_{ab} - J_{cd} + J_{ac} + J_{bd} = 2.745 \\
{}^{1}\Delta < \mathbf{H} >_{H} &= -J_{ad} - J_{bc} + J_{ac} + J_{bd} = -5.945
\end{aligned} \tag{S21b}$$

These equations are utilized for computations of J values under the classical approximation.

$$\begin{aligned}
J_{ab} &= ({}^{1}\Delta < \mathbf{H} >_{H} - {}^{3}\Delta < \mathbf{H} >_{D} - {}^{3}\Delta < \mathbf{H} >_{E}) / 2 = 0.00(0.00) \\
J_{ac} &= ({}^{3}\Delta < \mathbf{H} >_{D} + {}^{3}\Delta < \mathbf{H} >_{B} - {}^{5}\Delta < \mathbf{H} >_{A}) / 2 = -0.01(-0.01) \\
J_{ad} &= ({}^{3}\Delta < \mathbf{H} >_{E} + {}^{3}\Delta < \mathbf{H} >_{B} - {}^{1}\Delta < \mathbf{H} >_{H} - {}^{5}\Delta < \mathbf{H} >_{A}) / 2 = 0.00(0.00) \\
J_{bc} &= ({}^{3}\Delta < \mathbf{H} >_{D} + {}^{3}\Delta < \mathbf{H} >_{C} - {}^{1}\Delta < \mathbf{H} >_{H} - {}^{5}\Delta < \mathbf{H} >_{A}) / 2 = 6.36(6.13) \\
J_{bd} &= ({}^{3}\Delta < \mathbf{H} >_{C} + {}^{3}\Delta < \mathbf{H} >_{E} - {}^{5}\Delta < \mathbf{H} >_{A}) / 2 = 0.42(0.43) \\
J_{cd} &= ({}^{1}\Delta < \mathbf{H} >_{H} - {}^{3}\Delta < \mathbf{H} >_{B} - {}^{3}\Delta < \mathbf{H} >_{C}) / 2 = -2.33(-2.02)
\end{aligned} \tag{S22b}$$

As expected energy levels in section II.1, Jbc is largely positive in sign, indicating the greater stability of the triplet pair $(\uparrow \bullet O_1)(\uparrow \bullet Ru_1)$. The singlet-triplet gap for this pair is about 2J = 12.8 kcal/mol, that is smaller than the isoelectronic molecular oxygen (22.4 kcal/mol) and the iron-oxo species (about 18 kcal/mol).

The spin contamination errors in the BS solutions are usually neglected (22-24). However, the quantum corrections are not negligible as shown in Fig. S3 and S4. Therefore they are explicitly evaluated in bi-, tr- and tetra-radical species that play crucial roles in water splitting reaction in artificial and native PSII systems.

Figure Legends

Fig. S1. The ground (G), one ET (ETI and ETII) and double ET configurations for donor(D)–acceptor(A) systems (45, S1, S2):A) closed-shell configuration for DA complex, B) doubly electron-transfer (DET) configuration (++DA--), C) down-spin one-electron (OET) transfer configuration ETI and D) down-spin one-electron (OET) transfer configuration ETII.

Fig. S2. Energy levels for the ground (G), one ET (ETI, ETII) and double ET (DET) configurations before (b) and after (a) approximate spin projection (AP) or resonating

BS (RBS) CI: (A) nonradical ground state, (B) singlet ET (ET(S)) ground state ($J < 0$) and (C) triplet ET (ET(T)) ground state ($J > 0$). J is the effective exchange integral (S8). MLCT denotes the metal (M) - ligand (L) charge-transfer (CT) excitation in transition-metal cokmplexes.

Fig. S3. The energy levels for diradical species in Fig. 1 obtained by the broken-symmetry (BS) UB3LYP method (b-AP) and the improved energy levels after approximate spin projection (a-AP) that eliminates the spin contamination for BS UB3LYP solution (7-10). The AP effect is remakable for the 1,2-diradical configuration (^{X}C: X=1,3) that has the strong ferromagnetic effective exchange integral. The singlet-triplet energy (S-T) gap is small for the 1,3-diradical (^{X}B: X=1,3) because of small ferromagnetic exchange integral. The singlet state becomes the ground state for the Ru(III)-semi-quinone pair: (^{X}A: X=1,3) with the moderate orbital overlap.

Fig. S4. The energy levels for hexaradical species (**2ee**) in Fig. 2B obtained by the broken-symmetry (BS) UB3LYP method (b-AP) and the improved energy levels after approximate spin projection (a-AP) that eliminates the spin contamination in BS UB3LYP (7-10). The b- and a-AP denote before and after quantum spin (AP) correction. The lowest singlet (^{1}A) and triplet (^{3}A) configurations have, respectively, the local singlet diradical (LSD) and local triplet diradical (LTD) configutations for the O• •O radical pair. The energy gap between singlet and triplet states (^{X}A: X=1,3) of **2ee** is very samll, indicating the facile spin inversion (SI) (^{3}**4** -> ^{1}**5**) for the O-O bond formation in Fig. S7.

Fig. S5. The broken-symmetry (BS) orbitals obtained by hybrid DFT computations are transformed into the HOMO-LUMO mixing form as shown in eqs. S2a and S2b, though the HOMO and LUMO are obtained by the diagonalization of the first order density matrix of BS DFT. Therefore the molecular orbital (MO) obtained by this transformation is often specified as natural molecular orbital (NO): HOMO(=HONO) and LUMO(=LUNO). On the other hand, the eigen value of the diagonalized density matrix is referred to as the occupation number (n) that chemically means the population of electrons over HONO and LUNO: n(HONO) + n(LUNO) = 2.0. This figure illustrates the HONO(and next HONO(=HONO+1) and LUNO (and next LUNO (=LUNO+1) and their occupation numbers of the double one ET intermediate (**2bb**) with the antiferromagnetic (AF) spin configuration ($\downarrow$•SQ$_2$)($\uparrow$•Ru$_2$)($\uparrow$•Ru$_1$)($\downarrow$•SQ$_1$) (^{1}H in Fig. 3). The orbital overlaps (T) for the magnetic orbitals for ($\uparrow$•Ru$_1$)($\downarrow$•SQ$_1$) and

(↓•SQ_2)(↑•Ru_2) are 0.40 (=n(HONO)-1.0) and 0.55(=n(HONO+1)-1.0), respectively (see, main text).

Fig. S6. The definitions of HONO and LUNO and the transformation procedure for the first-order density matrix to obtain them are given in figure caption of Fig. S6. This figure illustrates the HONO(and next HONO(=HONO+1) and LUNO (and next LUNO(=LUNO+1) and their occupation numbers of the double one ET intermediate (**3a(+)ee**) with the antiferromagnetic (AF) spin configuration (↓•SQ_2)(↑•O_1)(↑•Ru_1)(↓•SQ_1) (^{1}H in Fig. 3). The orbital overlaps for the HONO-LUNO mixed orbitals (see eq. S2a and S2b) for (↓•SQ_2)(↑•O_1) and (↑•Ru_1)(↓•SQ_1) are 0.00(=n(HONO) – 1.0) and 0.38 (= n(HONO+1) – 1.0) , respectively (see, main text). The former complete HONO and LUNO mixing provides the localized orbitals in the left quinone and right O-Ru sites, respectively. These localized orbitals are chemically regarded as radical orbitals. On the other hand, the (HONO+1)-(LUNO-1) mixing is intermediate, giving more or less delolaized biradical orbitals for (↑•Ru_1)(↓•SQ_1). These are therefore referred to as “diradicaloid” orbitals in organic chemistry.

Fig. S7. A refined radical coupling (RC) mechanism for water splitting reaction by Tanaka catalyst: binuclear [Ru_2(btpyan)(3,6-di-$Bu_2Q)_2(OH_2)](SbF_6)_2$(**2**) (see, main text) The oxygen site of the Ru-oxo bond is usually regarded as oxygen dianion as shown in ^{1}**2** in conformity with the basic concept in organometallic chemistry. However, one electron transfer (OET) from the oxygen dianion to quinone group (Q) is a characteristic of Tanaka catalyst as shown in ^{1}**3** that is a tetraradical with the four spin 1/2 sites as in the case of four manganese ions of $CaMn_4O_5$ at OEC of PSII (eq. 1 in the text). This enables us to describe artificial and native OEC with the same spin Hamiltonian model as shown in the text (see Fig. 3) and our recent papers (7-10). The removal of two electrons from ^{1}**3** provides a formally Ru(IV)=O bond with oxygen dianion, but it is not the ground configuration. Indeed, the closed-shell Ru(IV)=O is less stable than the open-shell •Ru(III)-O• configuration ^{3}**4** in the case of Tanaka catalyst. Similarly the high-valent Mn(V)=O bond is reorganized into •Mn(IV)=O• as shown in our early theoretical paper (45). Such reorganization of the high-valent Mn-O bonds in OEC of PSII has been elucidated by the EXAFS experiments by Berkeley group (3,35) and recent DFT calculations of Siegbahn (42,43) and ours (44). Thus oxygen activation by the high-valent Ru(IV) and Mn(IV/V) ions is common in artificial (**2**) and native (**3**) water splitting systems (see main text). However the radical coupling is not possible for local triplet diradical (LTD) configuration in ^{3}**4**, indicating the spin inversion (SI) to generate local singlet diradical (LSD) configuration for the O-O bond formation as illustrated in ^{1}**5**. The spin alignments are also important for the steps (^{1}**7**-^{1}**9**) of the release of triplet (ground state) molecular oxygen from the singlet peroxide ^{1}**6**. The intracluster spin exchange (SE) accompanied by one electron transfer (OET) is necessary for the process. Thus spin degree of freedom plays important roles for Tanaka catalyst, supporting a spin Hamiltonian approach in the text.

Table Legends

Table S1. Mulliken spin densities of eight spin states of **2bb** at the B3LYP level
Table S2. Mulliken spin densities of eight spin states of **2a(+)ee** at the B3LYP level

Table S1. Mulliken spin densities of eight spin states of **2bb** at the B3LYP level

spin state	Ru1	Ru2	SQ1	SQ2	tpy	O1H	O2H
^{5}A	0.73	0.79	0.99	1.02	0.01	0.28	0.18
^{3}B	0.72	0.61	0.99	–0.75	–0.01	0.28	0.15
^{3}C	0.72	–0.61	0.99	0.75	0.02	0.27	–0.15
^{3}D	–0.59	0.79	0.85	1.02	0.01	–0.25	0.18
^{3}E	0.59	0.79	–0.85	1.02	0.00	0.27	0.18
^{1}F	0.73	–0.79	0.99	–1.02	0.01	0.27	–0.18
^{1}G	0.59	–0.61	–0.85	0.75	0.01	0.26	–0.15
^{1}H	0.59	0.61	–0.85	–0.75	–0.02	0.27	0.16

Table S2. Mulliken spin densities of eight spin states of **2a(+)ee** at the B3LYP level

spin state	Ru1	Ru2	SQ1	SQ2	tpy	O1	O2H$_2$
^{5}A	1.03	0.12	1.03	0.89	0.05	0.88	0.00
^{3}B	1.03	–0.12	1.03	–0.89	0.06	0.88	0.00
^{3}C	0.00	0.12	0.96	0.89	–0.02	0.06	0.00
^{3}D	0.05	0.12	0.91	0.89	0.03	0.01	0.00
^{3}E	0.96	0.12	–0.87	0.89	0.03	0.87	0.00
^{1}F	0.00	–0.12	0.96	–0.89	–0.01	0.06	0.00

^{1}G	–0.05	0.12	–0.91	0.89	–0.04	–0.01	0.00
^{1}H	0.96	–0.12	–0.87	–0.89	0.04	0.87	0.00

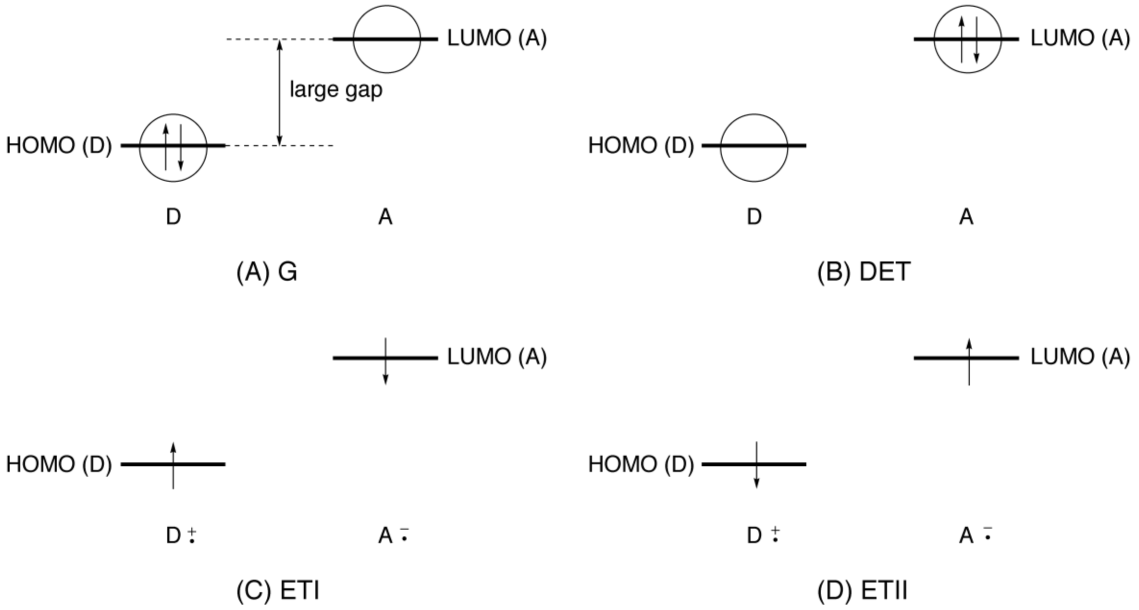

Fig. S1. The ground (G), one ET (ETI and ETII) and double ET configurations for donor(D)–acceptor(A) systems (45, S1, S2):A) closed-shell configuration for DA complex, B) doubly electron-transfer (DET) configuration (++DA--), C) down-spin one-electron (OET) transfer configuration ETI and D) down-spin one-electron (OET) transfer configuration ETII.

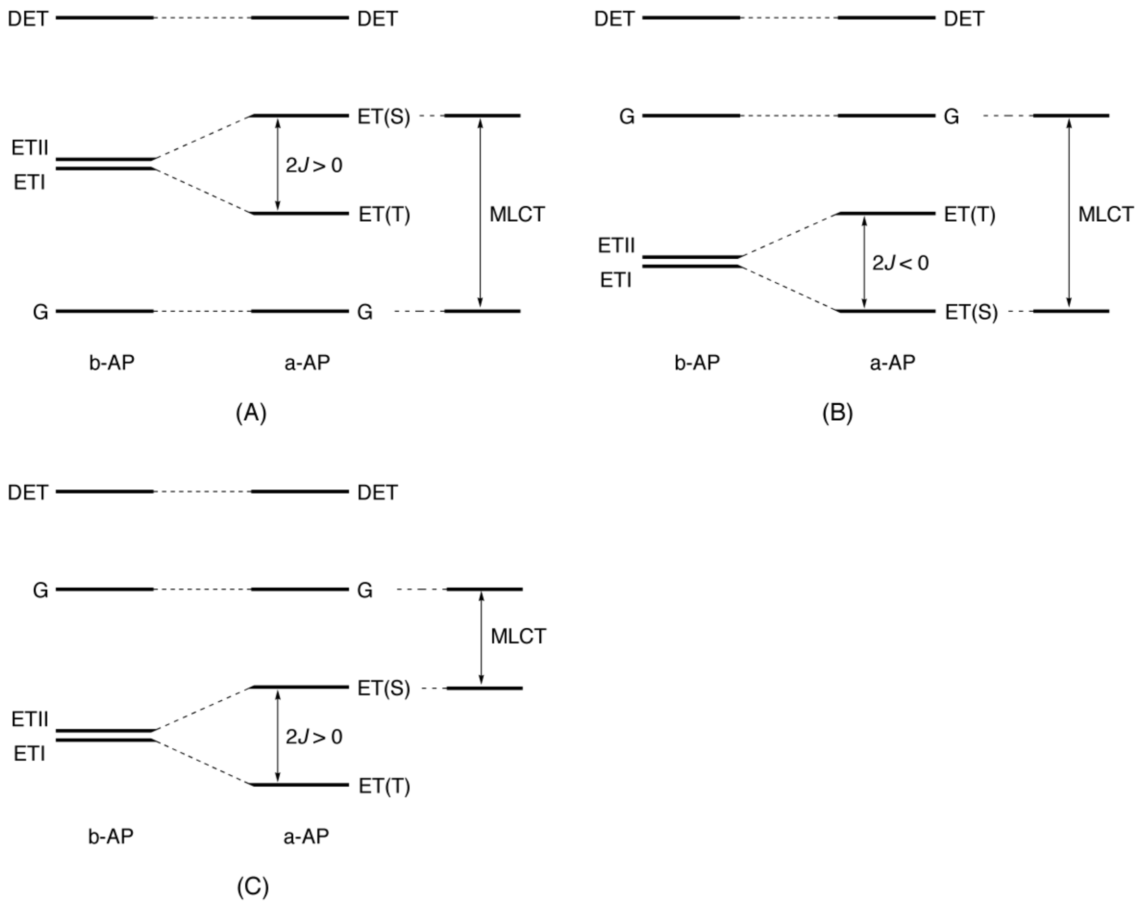

Fig. S2. Energy levels for the ground (G), one ET (ETI, ETII) and double ET (DET) configurations before (b) and after (a) approximate spin projection (AP) or resonating BS (RBS) CI: (A) nonradical ground state, (B) singlet ET (ET(S)) ground state ($J < 0$) and (C) triplet ET (ET(T)) ground state ($J > 0$). J is the effective exchange integral (S8). MLCT denotes the metal (M) - ligand (L) charge-transfer (CT) excitation in transition-metal cokmplexes.

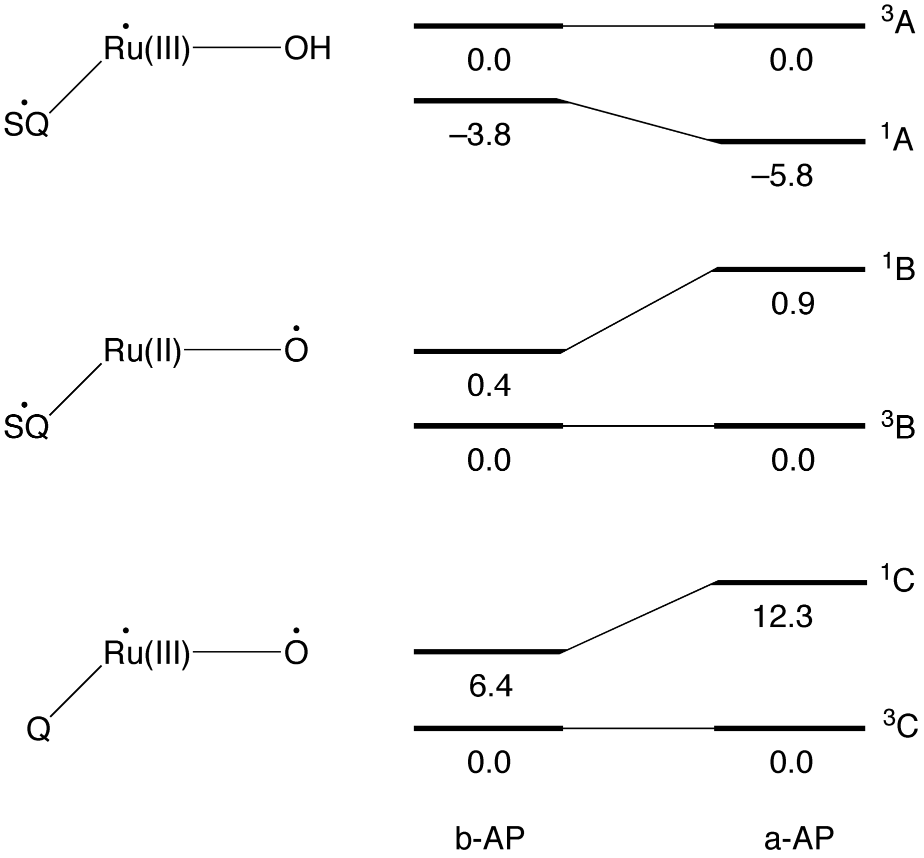

Fig. S3. The energy levels for diradical species in Fig. 1 obtained by the broken-symmetry (BS) UB3LYP method (b-AP) and the improved energy levels after approximate spin projection (a-AP) that eliminates the spin contamination for BS UB3LYP solution (7-10). The AP effect is remakable for the 1,2-diradical configuration (^{X}C: X=1,3) that has the strong ferromagnetic effective exchange integral. The singlet-triplet energy (S-T) gap is small for the 1,3-diradical (^{X}B: X=1,3) because of small ferromagnetic exchange integral. The singlet state becomes the ground state for the Ru(III)-semi-quinone pair: (^{X}A: X=1,3) with the moderate orbital overlap.

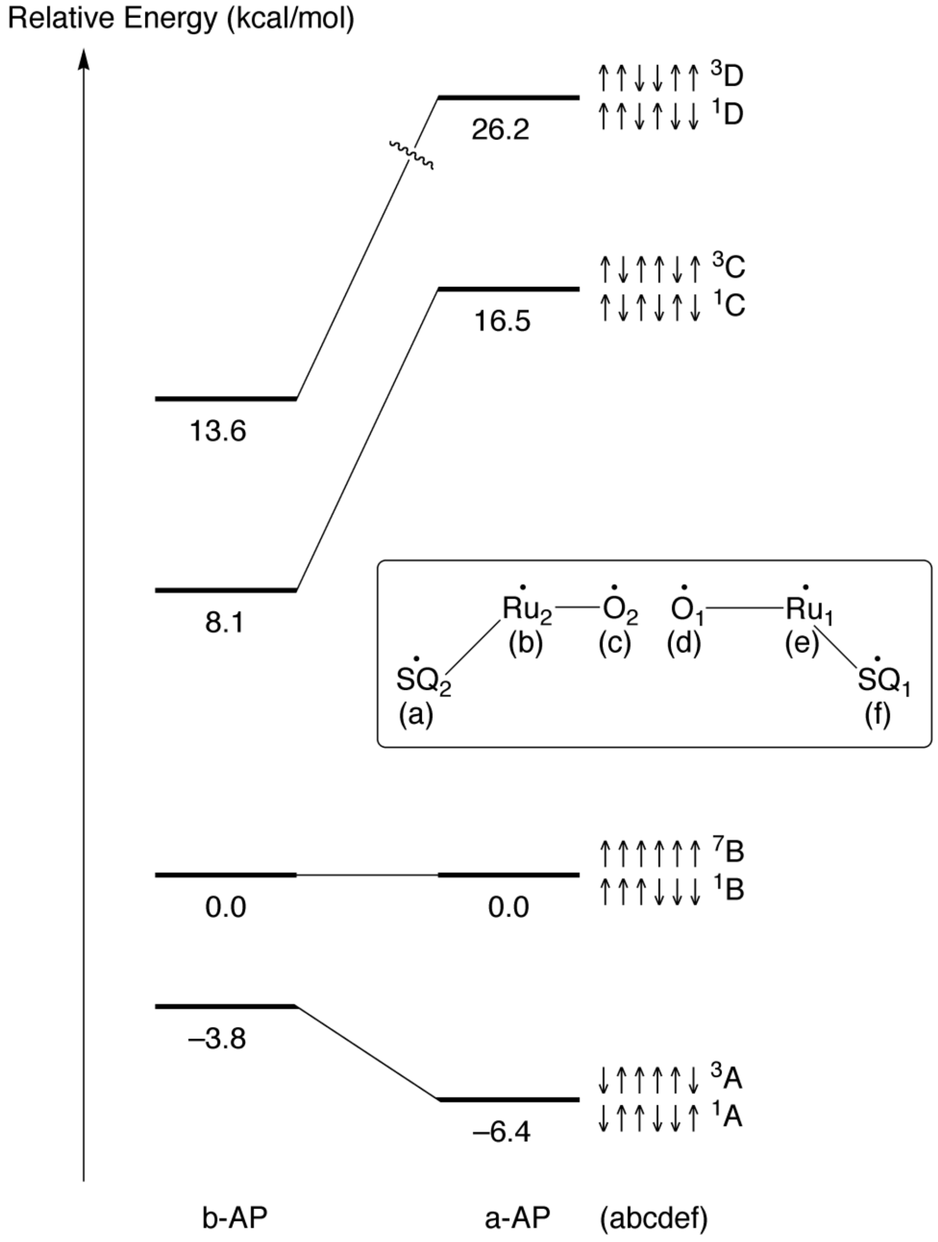

Fig. S4. The energy levels for hexaradical species (**2ee**) in Fig. 2B obtained by the broken-symmetry (BS) UB3LYP method (b-AP) and the improved energy levels after approximate spin projection (a-AP) that eliminates the spin contamination in BS UB3LYP (7-10). The b- and a-AP denote before and after quantum spin (AP) correction. The lowest singlet (^{1}A) and triplet (^{3}A) configurations have, respectively, the local singlet diradical (LSD) and local triplet diradical (LTD) configutations for the O• •O radical pair. The energy gap between singlet and triplet states (^{X}A: X=1,3) of **2ee** is very samll, indicating the facile spin inversion (SI) (^{3}**4** -> ^{1}**5**) for the O-O bond formation in Fig. S7.

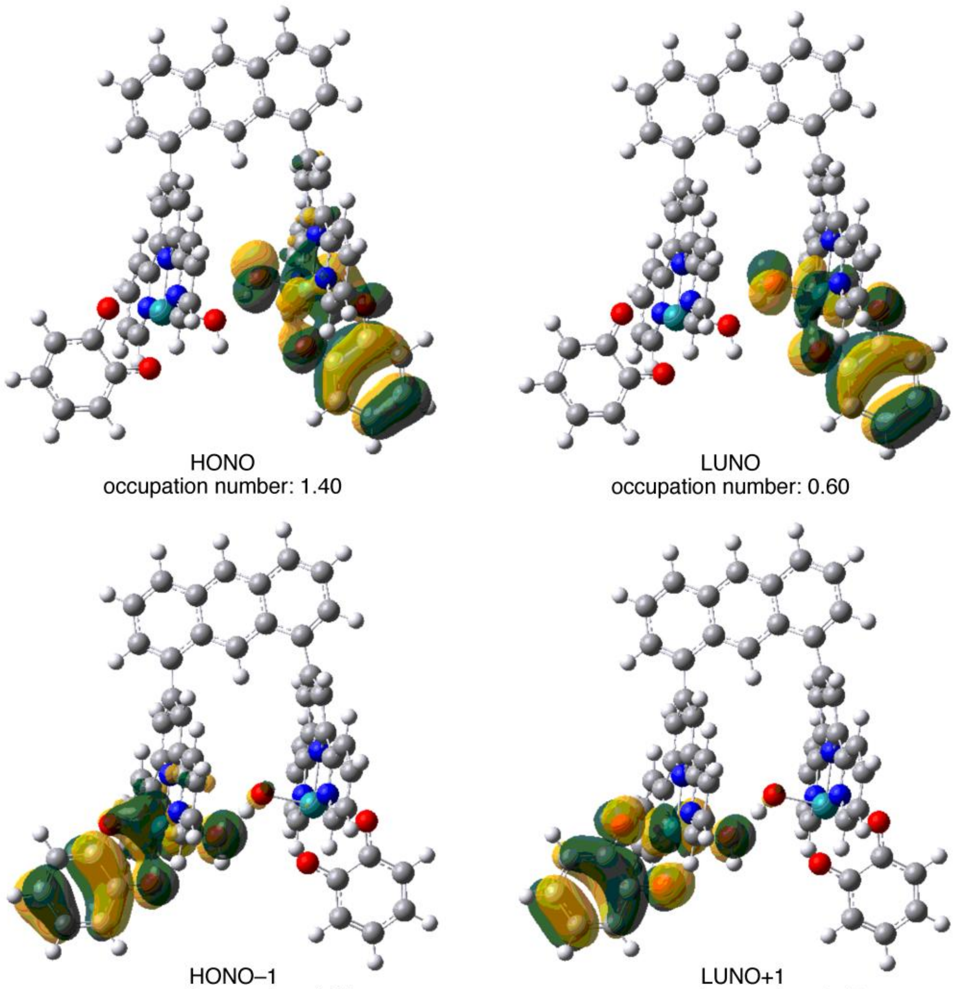

HONO
occupation number: 1.40

LUNO
occupation number: 0.60

HONO–1
occupation number: 1.55

LUNO+1
occupation number: 0.45

Fig. S5. The broken-symmetry (BS) orbitals obtained by hybrid DFT computations are transformed into the HOMO-LUMO mixing form as shown in eqs. S2a and S2b, though the HOMO and LUMO are obtained by the diagonalization of the first order density matrix of BS DFT. Therefore the molecular orbital (MO) obtained by this transformation is often specified as natural molecular orbital (NO): HOMO(=HONO) and LUMO(=LUNO). On the other hand, the eigen value of the diagonalized density matrix is referred to as the occupation number (n) that chemically means the population of electrons over HONO and LUNO: n(HONO) + n(LUNO) = 2.0. This figure illustrates the HONO(and next HONO(=HONO+1) and LUNO (and next LUNO (=LUNO+1) and their occupation numbers of the double one ET intermediate (**2bb**) with the antiferromagnetic (AF) spin configuration $(\downarrow\bullet SQ_2)(\uparrow\bullet Ru_2)(\uparrow\bullet Ru_1)(\downarrow\bullet SQ_1)$ (^{1}H in Fig. 3). The orbital overlaps (T) for the magnetic orbitals for $(\uparrow\bullet Ru_1)(\downarrow\bullet SQ_1)$ and $(\downarrow\bullet SQ_2)(\uparrow\bullet Ru_2)$ are 0.40 (=n(HONO)-1.0) and 0.55(=n(HONO+1)-1.0), respectively (see, main text).

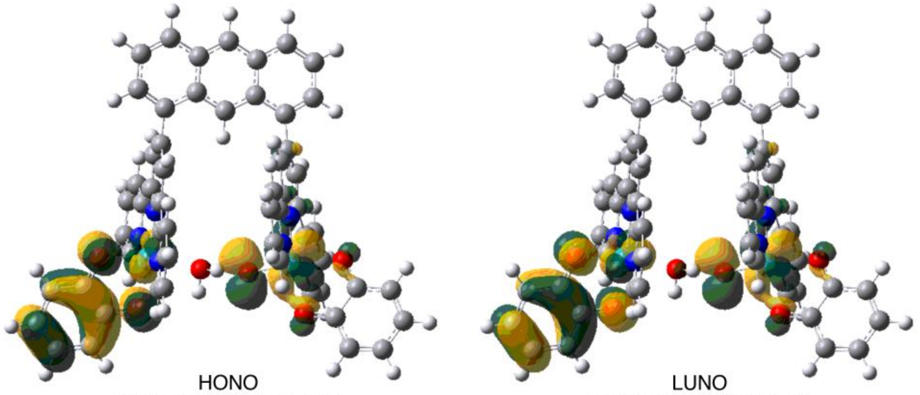

HONO
occupation number: 1.00

LUNO
occupation number: 1.00

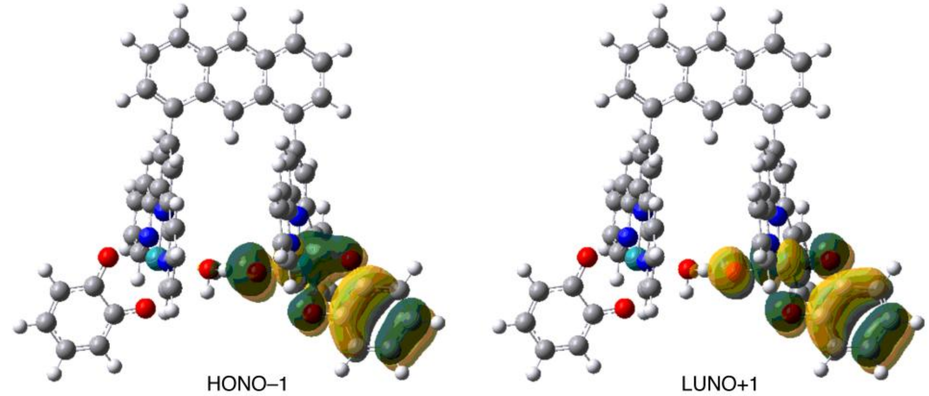

HONO–1
occupation number: 1.38

LUNO+1
occupation number: 0.62

Fig. S6. The definitions of HONO and LUNO and the transformation procedure for the first-order density matrix to obtain them are given in figure caption of Fig. S6. This figure illustrates the HONO(and next HONO(=HONO+1) and LUNO (and next LUNO(=LUNO+1) and their occupation numbers of the double one ET intermediate (**3a(+)ee**) with the antiferromagnetic (AF) spin configuration (↓•SQ$_2$)(↑•O$_1$) (↑•Ru$_1$)(↓•SQ$_1$) (^{1}H in Fig. 3). The orbital overlaps for the HONO-LUNO mixed orbitals (see eq. S2a and S2b) for (↓•SQ$_2$)(↑•O$_1$) and (↑•Ru$_1$)(↓•SQ$_1$) are 0.00(=n(HONO) – 1.0) and 0.38 (= n(HONO+1) – 1.0) , respectively (see, main text). The former complete HONO and LUNO mixing provides the localized orbitals in the left quinone and right O-Ru sites, respectively. These localized orbitals are chemically regarded as radical orbitals. On the other hand, the (HONO+1)-(LUNO-1) mixing is intermediate, giving more or less delolaized biradical orbitals for (↑•Ru$_1$)(↓•SQ$_1$). These are therefore referred to as “diradicaloid” orbitals in organic chemistry.

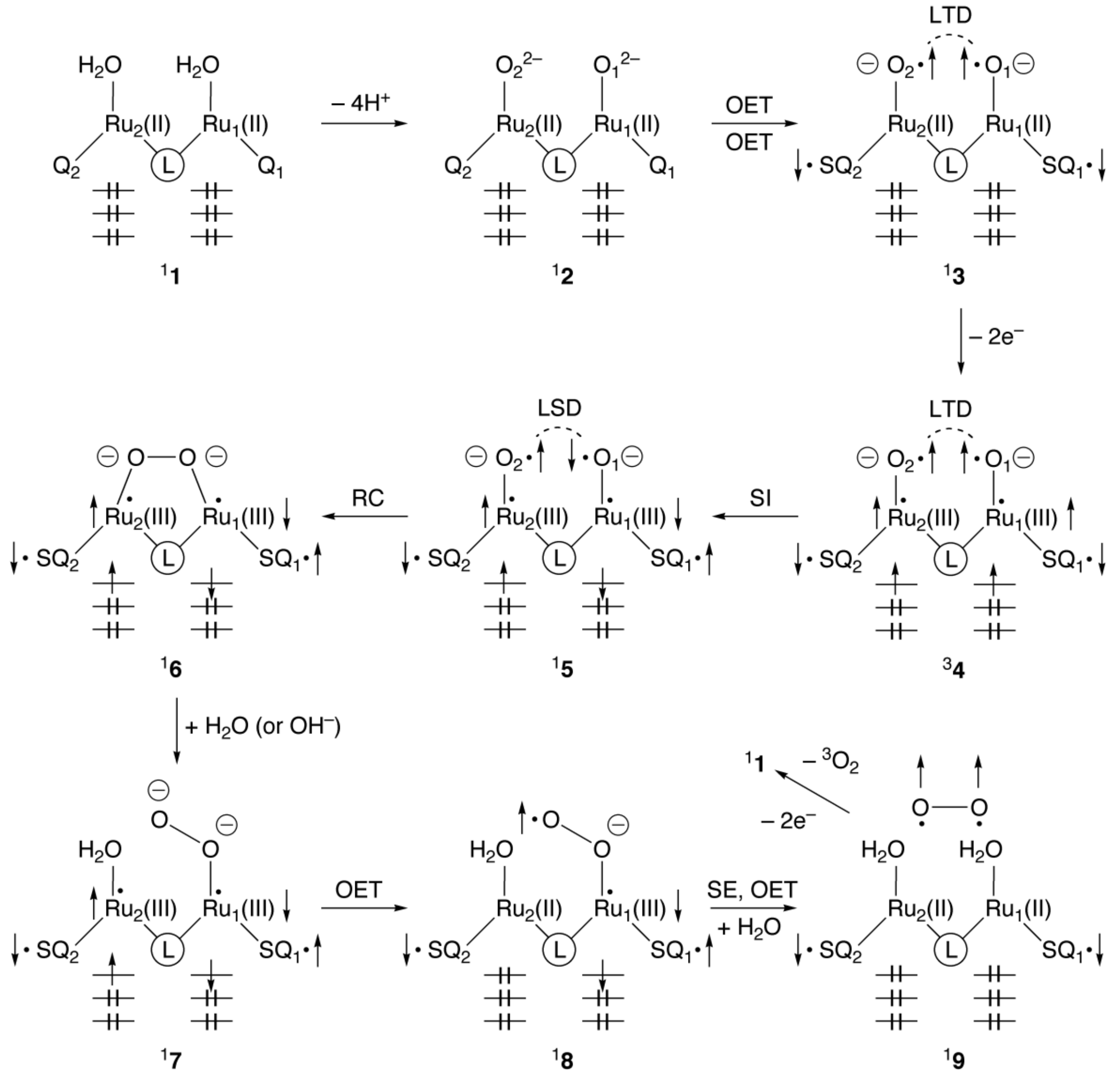

Fig. S7. A refined radical coupling (RC) mechanism for water splitting reaction by Tanaka catalyst: binuclear $[Ru_2(btpyan)(3,6\text{-di-}Bu_2Q)_2(OH_2)](SbF_6)_2$(**2**) (see, main text) The oxygen site of the Ru-oxo bond is usually regarded as oxygen dianion as shown in ^{1}**2** in conformity with the basic concept in organometallic chemistry. However, one electron transfer (OET) from the oxygen dianion to quinone group (Q) is a characteristic of Tanaka catalyst as shown in ^{1}**3** that is a tetraradical with the four spin 1/2 sites as in the case of four manganese ions of $CaMn_4O_5$ at OEC of PSII (eq. 1 in the text). This enables us to describe artificial and native OEC with the same spin Hamiltonian model as shown in the text (see Fig. 3) and our recent papers (7-10). The removal of two electrons from ^{1}**3** provides a formally Ru(IV)=O bond with oxygen dianion, but it is not the ground configuration. Indeed, the closed-shell Ru(IV)=O is less stable than the open-shell •Ru(III)-O• configuration ^{3}**4** in the case of Tanaka catalyst. Similarly the high-valent Mn(V)=O bond is reorganized into •Mn(IV)=O• as shown in our early theoretical paper (45). Such reorganization of the high-valent Mn-O bonds in OEC of PSII has been elucidated by the EXAFS experiments by Berkeley group (3,35) and recent DFT calculations of Siegbahn (42,43) and ours (44). Thus oxygen activation by the high-valent Ru(IV) and Mn(IV/V) ions is common in artificial (**2**) and native (**3**) water splitting systems (see main text). However the radical coupling is not possible for local triplet diradical (LTD) configuration in ^{3}**4**, indicating the spin inversion (SI) to generate local singlet diradical (LSD) configuration for the O-O bond formation as illustrated in ^{1}**5**. The spin alignments are also important for the steps (^{1}**7**-^{1}**9**) of the release of triplet (ground state) molecular oxygen from the singlet peroxide ^{1}**6**. The intracluster spin exchange (SE) accompanied by one electron transfer (OET) is necessary for the process. Thus spin degree of freedom plays important roles for Tanaka catalyst, supporting a spin Hamiltonian approach in the text.

.

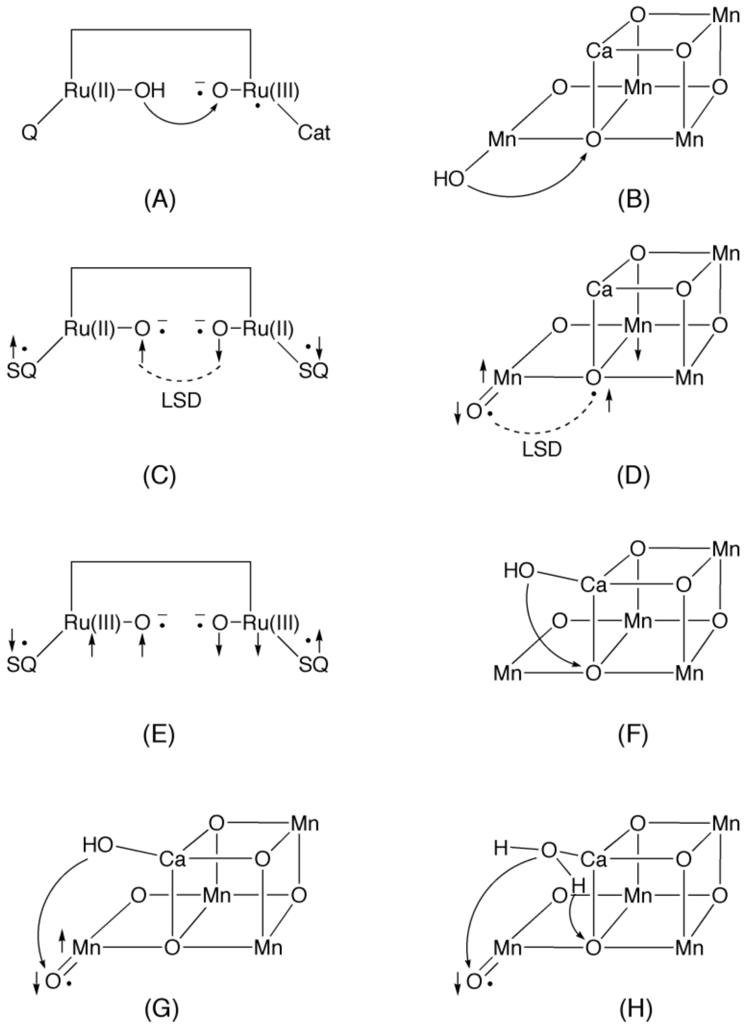

Fig. S8. Possible reactions pathways for the O-O bond formation in artificial (**2**) and native (**3**) water splitting systems (see, main text). (A) the nucleophilic attack of hydroxide anion coordinated to Ru(II) to the electrophilic oxygen of the Ru-oxo bond proposed by Muckerman et al (25), (B) the nucleophilic attack of hydroxide anion coordinated to Mn(IV) to the electrophilic oxygen of the Mn-O-Mn bond proposed by Yamaguchi et al (9,10), (C) early radical coupling model proposed by Tanaka et al (20,21), (D) a radical coupling model proposed for OEC of PSII by Kanda et al (7, 8), (E) the radical coupling model proposed by Baik et al (22-24) on the theoretical grounds and by Tanaka et al on the new experimental result (34), (F) the nucleophilic attack of hydroxide anion coordinated to Ca(II) to the electrophilic oxygen of the Mn-O-Mn bond proposed by Yamaguchi et al (9,10), (G) the nucleophilic attack of hydroxide anion coordinated to Ca(II) to the electrophilic oxygen of the newly formed Mn-oxo bond proposed by Yamaguchi et al (9,10), and (H) the nucleophilic attack of water molecule coordinated to Ca(II) to the electrophilic oxygen of the newly formed Mn-oxo bond assisted with proton accepting oxygen dianion proposed by Yamaguchi et al (9,10). Baber (1,36) et al have proposed the radical/nuclephilic attack (G) model on their X-ray structure (1,36). The DFT calculations (7-10) have elucidated that the acid-base type mechanisms (F, G, H) for OEC of PSII become favorable because of the participation of the Ca(II) ion that remains divalent throughout the reaction. Therefore the Mn-Ca pair in the native OEC of PSII is different from the Mn-Mn pair in the model (A) for Tanaka catalyst. Moreover the reaction field in Tanaka catalyst is not so hydrophilic, giving no stabilization of the acid-base mechanism by extra water molecules in contrast to Blue dimmers by Meyer et al (13,14,15). This is the reason why the radical coupling models (C and D) become favorable for Tanaka catalyst on both experimental (34) and theoretical (22-24) grounds. The antiferromagnetic spin coupling in artificial and native OEC systems is crucial for formation of local singlet diradical (LSD) configuration for the O-O bond formation of generated oxygen radical sites as illustrated in C and D. On the other hand, the ferromagnetic exchange coupling is essential for generation of triplet molecular oxygen as discussed in detail in the refs. 7-10 and 44.